INTERNATIONAL SCIENTIFIC JOURNAL

MATHEMATICAL MODELING

YEAR IY, ISSUE 3/2020
ISSN (PRINT) 2535-0986
ISSN (WEB) 2603-2929

Published by
SCIENTIFIC-TECHNICAL UNION of MECHANICAL ENGINEERING - INDUSTRY 4.0
Sofia, BULGARIA

INTERNATIONAL SCIENTIFIC JOURNAL

MATHEMATICAL MODELING

PUBLISHER:

SCIENTIFIC TECHNICAL UNION OF MECHANICAL ENGINEERING
"INDUSTRY 4.0"

108, Rakovski Str., 1000 Sofia, Bulgaria
tel. (+359 2) 987 72 90,
tel./fax (+359 2) 986 22 40,
office@stumejournals.com
www.stumejournals.com

ISSN (PRINT) 2535-0986
ISSN (WEB) 2603-2929
YEAR IV, ISSUE 3 / 2020

CONTENTS

Stability of convective motion of a fluid with impurity

Prof., Dr. Dementev O.[1], PhD. Turlakova S.[2]
Chelyabinsk State University, Chelyabinsk, Russia[1], South Ural National Research University, Chelyabinsk, Russia[2]
e-mail: dement@csu.ru[1], turlakovasu@susu.ru[2]

Abstract: *The problem of convective stability in a medium containing settling heavy solid particles are discussed. A study is made of the stability of steady convective flow of a medium containing an additive between vertical plates heated to different temperatures. It is shown that the presence of settling solid particles has a significant stabilizing effect on convective stability.*
Keywords: STEADY-STATE CONVECTIVE FLOW, STABILITY, LIQUID, HEAVY IMPURITY

1. The transporting medium and the additive were considered as interpenetrating and interacting continuous media; interaction between particles was neglected. A formulation of the problem of flow stability based on these concepts was first given in [1] where stability of motion in a plane vertical channel was considered for a fluid containing an additive. The stability of convective motion of a medium transporting a solid additive in a layer between vertical heated to different temperatures was studied in [5] where the settling of the particles was neglected, as was the case in [2-4].

Particle setting and the displacement force acting on the particles were neglected. The existence of thermal equilibrium between particles and gas was assumed, i.e., the simple limiting case of an infinitely short temperature relaxation time τ_t was considered. Under the assumptions described, the effect of the particles present in a layer reduced to a mere renormalization of the heat capacity of the gas and so to a trivial renormalization of the Rayleigh number also. A study is made of the effect on convective of all factors characterizing the added particles: the rate of particle settling u_s, the velocity and temperature relaxation times for the particles (or, which comes to the same thing, their size, density, and heat capacity), and the mass concentration of the additive.

2. We consider a viscous incompressible fluid containing a cloud of spherical nondeformable solid particles of identical radius *r* and mass *m*. As in [1-6], we assume the liquid and impurity to be continuous media, interpenetrating and interacting with each other, and neglect interaction between the particles. The volume fraction of particles is assumed to be so low that the Einstein correction to liquid viscosity can be neglected. The density of the particle material ρ_1 is much greater than the density of the carrier medium ρ. The left force acting on the particles is negligibly small, since it is proportional to the ratio $\rho/\rho_1 \ll 1$. Interaction between the phases as they undergo relative motion follows the Stokes law. The equations describing the behaviour of an incompressible fluid with an impurity of heavy solid particles have the form [7, 8]. Based on those equations, equations were obtained [6] in the Boussinesq approximation for the free convection of an incompressible medium with a heavy additive:

$$\frac{\partial \vec{u}}{\partial t} + (\vec{u}\nabla)\vec{u} = -\frac{\nabla p}{\rho} + \nu\Delta\vec{u} - \frac{a}{\tau_\nu}\left(\vec{u}_p - \vec{u}\right) + (1+a)\vec{g}\beta T,$$
$$\frac{\partial \vec{u}_p}{\partial t} + \left((\vec{u}_p + \vec{u}_s)\nabla\right)\vec{u}_p = \frac{1}{\tau_\nu}\left(\vec{u}_p - \vec{u}\right),$$
$$\frac{\partial T}{\partial t} + (\vec{u}\nabla)T = \chi\Delta T + \frac{ab}{\tau_t}\left(T_p - T\right), \qquad (1)$$
$$\frac{\partial T_p}{\partial t} + ((\vec{u}_p + \vec{u}_s)\nabla)T_p = -\frac{1}{\tau_\nu}\left(T_p - T\right),$$
$$div\,\vec{u} = 0,\ \ \frac{\partial \rho_p}{\partial t} + div\left(\rho_p(\vec{u}_p + \vec{u}_s)\right) = 0,$$

$$\rho_p = mN,\ \tau_\nu = \frac{m}{6\pi r\rho\nu},\ \tau_t = \frac{mb}{4\pi r\rho\chi},\ a = \frac{\rho_p}{\rho},$$

where $\vec{u}$ is the liquid velocity; *T* is temperature; *p* is pressure of the fluid measured with respect to the hydrostatic pressure renormalized because of the settling particles; *c* is the heat capacity of the fluid at constant pressure; *β*, *ν* and *χ* are the coefficient of volume expansion of the fluid, its kinematic viscosity, and thermal diffusivity; quantities with the subscript "*p*" refer to the particle cloud, where $\vec{u}_p$ is the velocity acquired by the particles as a result of their interaction with the moving fluid measured with respect to the rate of particle settling $\vec{u}_s$; c_1 is the heat capacity of the particle material; *N*, number of particles per unit volume; and $\vec{g}$, acceleration of gravity. The quantities τ_t and τ_ν have the dimensionality of time and are, respectively, the time required for the temperature difference between fluid and particles to decrease by factor *e* and the time required for the velocity of the particles relative to the fluid to decrease by factor of *e* in comparison with its original value.

We consider isothermal motion of incompressible fluid containing an additive in a plane layer between infinite parallel vertical surfaces at $x = \pm h$, which are maintained at the constant temperature Θ, respectively. The particles, the concentration of which is not uniform, move through the fluid.

We obtain a steady-state solution of the equation system (1) describing plane-parallel convective motion in such a structure,

$$u_x = u_y = 0,\ u_z = u_0(x),\ T_0 = const,\ p_0 = p_0(z),$$
$$u_{px}=u_{py}=0,\ u_{pz}=u_{p0}(x),\ T_{p0} = const, \qquad (2)$$
$$N(\alpha,x) = \frac{4ch\,\alpha\ ch\,\frac{\alpha x}{h} - ch\,\frac{2\alpha x}{h} - ch\,2\alpha - 2}{4ch\,\alpha - ch\,2\alpha - 3},$$

where α is a coefficient defining the impurity concentration near the boundary of the layer. Equation (2) describes well the distribution of settling particles in a vertical channel observed experimentally in [8].

The settling particles, nonuniformly distributed across the channel, interact with the liquid and set it in motion. We find the steady-state distribution of liquid and particle velocities from Eq. (l) with the assumption that trajectories of both liquid and solid particles are straight lines parallel to the *z* axis, closing at infinity above and below:

$$\frac{1}{\rho}\frac{dp_0}{dz} = \nu\frac{d^2u_0}{dx^2} - \frac{a}{\tau_\nu}\left(u_{p0} - u_0\right) - g,$$
$$\frac{1}{\tau_\nu}\left(u_{p0} - u_0\right) = g. \qquad (3)$$

Here is u_0 and u_{p0} are the vertical velocity components and the subscript 0 indicates the steady-state solution of Eq. (1).

The boundary conditions and closed flow condition are expressed by

$$u(\pm 1) = 0, \quad \int_{-h}^{h} u_0 dx = 0. \tag{4}$$

Solving the problem of Eqs. (3), (4), we obtain the steady-state distributions of liquid and particle cloud velocities over the layer section

$$\begin{aligned}
&u_0 = \frac{gh^2}{\nu} B_1 \left[\frac{1}{\alpha^2} \left(4ch\,\alpha\, ch\,\frac{\alpha x}{h} - \frac{1}{4} ch\,\frac{2\alpha x}{h} \right) + B_2 \frac{x^2}{h^2} - B_3 \right], \\
&u_{p0} = u_0 - g\tau_\nu, \; \nabla p_0 = const, \\
&B_1 = \frac{m}{\rho(4ch\,\alpha - ch\,2\alpha - 3)}, \\
&B_2 = \frac{3}{4\alpha^2} \left(\frac{15}{4\alpha} sh\,2\alpha - \frac{7}{2} ch\,2\alpha - 4 \right), \\
&B_3 = \frac{45}{16\alpha^3} sh\,2\alpha - \frac{7}{8\alpha^2} ch\,2\alpha - \frac{1}{\alpha^2}.
\end{aligned} \tag{5}$$

As is evident from Eq. (5), under the action of the settling particles within the layer a liquid motion is established with two ascending and one descending flow, symmetric about the z axis. The intensity of the motion decreases with increase in α (as $\alpha \to \infty$, $u_0 \to 0$).

We will study the stability of the steady-state liquid flow of Eq. (5), produced by settling of the nonuniformly distributed impurity particles. To do this we impose upon the steady-state velocity fields u_0, u_{p0}, pressure p_0, and number of particles per unit volume N_0, the small perturbations u, u_p, p, N.

We write the equations for the perturbations in dimensionless form, using the following units to dedimensionalize: for distance, h; time, h^2/ν; velocity, ν/h; pressure $\rho\nu^2/h^2$. Linearizing with respect to the perturbations, we obtain from Eq. (1).

$$\begin{aligned}
&\frac{\partial \vec{u}}{\partial t} (\vec{u}_0 \nabla)\vec{u} + (\vec{u}\nabla)\vec{u}_0 = \nabla p + \Delta \vec{u} - \frac{\vec{u}_0}{\tau_\nu}(\vec{u}_p - \vec{u}) + Ga\vec{\gamma}, \\
&\frac{\partial \vec{u}_p}{\partial t} + (\vec{u}_{p0}\nabla)\vec{u}_p + (\vec{u}_p \nabla)\vec{u}_{p0} = \frac{1}{\tau_\nu}(\vec{u}_p - \vec{u}), \\
&\frac{\partial N}{\partial t} + div(N_0 \vec{u}_0 + N\vec{u}_{po}) = 0; \\
&div\,\vec{u} = 0;
\end{aligned} \tag{6}$$

$$\begin{aligned}
&u_0 = GB_1 \left[\frac{1}{\alpha^2} \left(4ch\,\alpha\, ch\,\alpha x - \frac{1}{4} ch\,2\alpha x \right) + B_2 x^2 - B_3 \right], \\
&u_{p0} = u_0 - u_S, \; \vec{u}_S = -G\tau_\nu \vec{\gamma}, \\
&\tau_\nu = \frac{2}{9} r^2 \frac{\rho_1}{\rho}, \; a = \frac{mN}{\rho}, \; a_0 = \frac{mN_0}{\rho}, \; G = \frac{gh^3}{\nu^2}, \\
&N_0 = \frac{4\,ch\,\alpha\, ch\,\alpha x - ch\,2\alpha x - ch\,2\alpha - 2}{4ch\,\alpha - ch\,2\alpha - 3},
\end{aligned} \tag{7}$$

where u_s is the particle settling velocity; G is the Galileo number; τ_ν is the dimensionless relaxation time; $\vec{\gamma}$ is a unit vector directed vertically upward.

For a liquid with impurity [6, 10], as for a pure liquid [9], it has been demonstrated at the problem of stability with respect to spatial perturbations reduces to the problem of stability with respect to planar perturbations. In the case under consideration planar perturbations are more dangerous, i.e., they correspond to lower Galileo numbers, so that in studying stability it is sufficient to limit ourselves to the study of planar normal perturbation:

$$\begin{aligned}
&\vec{u}_p(x,z,t) = \vec{v}_p(x)\exp[ik(z - ct)], \\
&N(x,z,t) = n(x)\exp[ik(z - ct)], \\
&\Psi(x,z,t) = \varphi(x)\exp[ik(z - ct)], \\
&u_x = -\frac{\partial \Psi}{\partial z}, \; u_z = \frac{\partial \Psi}{\partial x}.
\end{aligned} \tag{8}$$

Here Ψ is the flow function; φ, v_p, n are the perturbation amplitudes; κ is the real wave number; $c = c_r + ic_i$ is the complex phase velocity of the perturbations (c_r is the phase velocity, c_i is the decrement).

$$\begin{aligned}
&\left(\varphi^{IV} - 2k^2\varphi'' + k^4\varphi\right) + ik\left(\varphi'' - k^2\varphi\right)\left(c - u_0 + \frac{a_0}{ik\tau_\nu}\right) + \\
&+ iku_0''\varphi = \frac{a_0}{\tau_\nu}\left(v_{pz}' - \varphi'\right) + Gn', \\
&v_{px} = \frac{ik\varphi}{ik\tau_\nu(up_0 - c) - 1}, \\
&v_{pz} = \frac{-\varphi' + u_{p0}'\tau_\nu v_{px}}{ik\tau_\nu(up_0 - c) - 1}, \\
&n = \frac{ikv_{pz}N_0 + N_0' v_{px} + N_0 v_{px}}{ik(u_{p0} - c)}
\end{aligned} \tag{9}$$

with boundary conditions

$$\varphi(\pm 1) = \varphi'(\pm 1) = 0. \tag{10}$$

The stability boundary for flow of the liquid with impurity Eq. (7) is determined by the condition $c_i = 0$. The complex phase velocity c depends on the problem parameters G, k, a, τ_ν. To solve the boundary problem Eqs. (9) and (10), i.e., to determine the stability limits of the flow under consideration and calculate the decrement spectrum, we use the Runge - Kutta method of step-by-step integration.

Calculations performed for a wide range of values of the parameter α $(0.5 \le \alpha \le 70)$ show that instability of steady-state motion of the liquid with heavy particles is caused by the interaction of oppositely directed flows: the descending central flow and two ascending flows near the walls. Instability in the motion is produced by lower modes of hydrodynamic perturbations, while the decrements of normal perturbations prove to be complex (traveling perturbations).

The settling particles generate oscillatory (traveling) perturbations and encourage their transport. With decrease in the parameter α the stability of the flow induced by particle settling decreases. In fact, at low α the particle distribution in the layer has a sharply expressed "tonguelike" character and the flow intensity is high; decrease in α leads to an increase in flow velocity and disruption of stability. This conclusion is confirmed by calculations of neutral stability curves ($c_i = 0$, $\tau_\nu = 0.009$, $\alpha_1 = 20$, $\alpha_2 = 30$, $\alpha_3 = 40$, $\alpha_4 = 45$, $\alpha_5 = 50$, $\alpha_6 = 65$). The character of the heavy particle distribution across the layer affects the stability of the flow induced by the impurity intensely.

3. We consider convective motion of a fluid containing an additive in a plane layer between infinite parallel vertical surfaces, which are constant temperatures – Θ and Θ, respectively. The particles, the concentration of which is nonuniform, move through the fluid. We obtain a steady-state solution of the equation, describing plane-parallel convective motion and we used boundary conditions $u_0(\pm h) = 0$, $T_0(-h) = \Theta$, $T_0(h) = -\Theta$ and the closure condition for convective flow. We obtain the distribution of velocities and temperatures of the fluid and particle cloud over a section layer:

$$U_0 = Gr\{\frac{x^3}{6} + \frac{m}{\rho_0(4ch\alpha - ch2\alpha - 3)}(\frac{4ch\,\alpha}{\alpha^2}(xch(\alpha x)$$
$$-\frac{2sh(\alpha x)}{\alpha}) - \frac{1}{4\alpha^2}(xch(2\alpha x) - \frac{2sh(2\alpha x)}{\alpha}) -$$
$$\frac{ch2\alpha + 2}{6}x^3) + C_1 x\} + u_0, \qquad (11)$$
$$U_{p0} = U_0 + u_s, T_0 = T_{po} = -x,$$

$$C_1 = -\frac{1}{6} - \frac{m}{\rho_0(4ch\alpha - ch2\alpha - 3)}(\frac{8ch\alpha}{\alpha^2}(ch\alpha -$$
$$\frac{2sh2\alpha}{\alpha}) - \frac{1}{2\alpha^2}(ch2\alpha - \frac{sh2\alpha}{\alpha}) - \frac{ch2\alpha + 2}{3});$$
$$\tau_t = \frac{3\Pr\tau_v b}{2}, b = \frac{C_1}{C}, \Pr = \frac{\nu}{\chi}, Gr = g\frac{g\beta\Theta h^3}{\nu^2}.$$

We write the equations in dimensionless form, using the following units of measurement: distance h, time h^2/ν, velocity ν/h, pressure $\rho\nu^2/h^2$, and temperature Θ.

4. The stability of convective motion. We investigate the stability of the steady-state motion of a medium containing a heavy additive as defined by Eqs. (11). To do this, we consider the perturbed fields for velocity, temperature, pressure and number of particles per unit volume.

As in the case of a pure fluid [9], one can show for a medium containing an additive that the problem of stability with respect to spatial perturbations reduces to the corresponding problem for plane perturbations. Plane perturbation are more dangerous in the case of vertical orientation of the layer, i.e., lower Grashof numbers Gr are associated with them. Consequently, it is sufficient to continue the investigation to plane perturbations in a study of stability.

We consider plane normal perturbations

$$N(x,z,t) = n(x)\exp[ik(z-ct)],$$
$$\Psi(x,z,t) = \varphi(x)\exp[ik(z-ct)],$$
$$u_{px}(x,z,t) = v_{px}(x)\exp[ik(z-ct)], \qquad (13)$$
$$u_{pz}(x,z,t) = v_{pz}(x)\exp[ik(z-ct)],$$
$$T(x,z,t) = \theta(x)\exp[ik(z-ct)],$$
$$u_x = -\frac{\partial\Psi}{\partial z}, u_z = \frac{\partial\Psi}{\partial x}.$$

Where ψ is a stream function; φ, Θ, n are the amplitudes of the perturbations. We obtain a system of amplitude equations (primes denote differentiation with respect to x)

$$(\varphi^{IV} - 2k^2\varphi'' + k^4\varphi) + ik(\varphi'' - k^2\varphi)\cdot$$
$$\left(c - u_0 + \frac{a_0}{ik\tau_\nu}(\frac{1}{A} - 1)\right) + \frac{a_0'\varphi'}{\tau_\nu}\left(\frac{1}{A} - 1\right) +$$
$$+\varphi(iku_0'' + \frac{ik}{A^2}(a_0 u_{p0}'' + a_0' u_{p0}') + \qquad (14)$$
$$\frac{2a_0 k^2\tau_\nu u'^2{}_{p0}}{A^3}) + (1 + a_0)Gr\cdot\vartheta' + a' =$$
$$= GrT + aGrT' + a_0' Gr\vartheta = 0,$$

$$\frac{1}{\Pr}(\vartheta'' - k^2\vartheta) + \vartheta(\frac{a_0 b}{\tau_t}(\frac{1}{B} - 1) + ik(c - u_0)) +$$
$$ik\varphi T'(\frac{a_0 b}{AB} + 1) = 0,$$

$$A = ik\tau_v(u_{p0} - c); B = ik\tau_t(u_{p0} - c) + 1;$$
$$n = \frac{\tau_v}{A-1}(\frac{2N_0 k^2\tau_v u_{p0}'\varphi}{A^2} + \frac{N_0' ik\varphi}{A}).$$

Boundary conditions are

$$\varphi(\pm 1) = \varphi'(\pm 1) = 0 \qquad (15)$$

The boundary-value problem (14) - (15) determines the spectrum of characteristic perturbations and their decrements. The complex phase velocity c depends on seven independent parameters of the problem: *Ga, Pr, Ga, k, a,* τ_v, τ_t, α. The limit of stability for steady-state flow is determined from the condition $c_i = 0$. To solve the resultant boundary-value problem, i.e. to determine the decrement spectrum and the flow stability limits, the Runge – Kutta - Merson method of stepwise integration was used with orthogonalization of solutions at each step in the integration. The method used made it possible to carry out calculations to sufficiently large valued of the problem parameters: $Gr \sim 10^6$, $Pr \sim 10^3$, $Ga \sim 10^6$.

The presence of added particles shows up primarity in the spectrum of perturbation decrements. In contrast to the spectrum for a layer of pure fluid and the spectrum for a layer with transverse seepage fluid, the perturbation spectrum is now considerably richer because of the appearance of perturbations associated with the particle cloud. As shown by calculations, however, perturbations associated with the transport medium remain responsible for the instability of the equilibrium state.

Transverse motion of the particles leads to a considerable change in the perturbation spectrum for a stationary layer of pure fluid. Oscillational perturbations now appear in the spectrum; they arise as the result of coalescence of real levels. With an increase in Rayleigh number, these complex-conjugate pairs break down into two real levels. Instability, as in the case of a stationary layer of pure fluid, is caused by the real branches of the spectrum and has monotone nature.

The effect of particle setting rate on the stability of a layer shows the dependence of the minimum critical number Ra_m on the particle setting rate u_s. Layer stability rises rapidly with increase in u_s. The wavelength of the most dangerous perturbations decreases. In a layer of air 2 cm thick, motion of wood particles at a velocity ≈ *25cm/sec (a = 0.15, r = 0.008 cm)* increase the stability by factor of almost 18. With an increase in the particle setting rate, however, the rate of rise in the minimum critical Rayleigh number slows down *(for* $|u_s| \geq$ *180).*

With an increase in particle setting rate, a thermal boundary layer begins to form at the lower boundary of the layer. As a result, the effective thickness of the stratified layer of gas is decreased $(h_{eff} < h)$. The characteristic temperature difference of 2Θ remains fixed in this case. The critical temperature difference is found from the condition $(1+a)g\beta\Theta\, h^3_{eff}/\nu\chi = const$ and therefore the critical Rayleigh number, which is determined in the usual manner from the halfwidth h of the layer, is increased in proportion to the decrease in h_{eff}, i.e., to the rise in $|u_s|$. This occurs as long as the particles "blowup" the distribution of gas temperature increase the thickness of the thermal boundary layer at the lower surface. It turns out that at high values of the setting rate, further increase leads to insignificant distortion of the established distribution of gas temperature and so to a small rise in stabilizing effect.

Intensification of the distorting effect of particles on the distribution of gas temperature is also observed when there is an increase in the mass concentration *a* of the additive. The stabilizing effect of the particles on equilibrium stability increases in this case. With an increase in the mass concentration *a* by a factor of two from 0.15 to 0.37, the minimum critical Rayleigh number increases from 780 to 203 5 and the critical wavenumber k_m increases from 2.2 to 2.9. Convective equilibrium stability in our case is much higher than the stability of a pure fluid. Stability rises with an increase in the relative heat capacity *b* of the particles. Particles having a higher heat capacity better absorb the perturbations that are the most dangerous.

The behavior of the minimum critical Rayleigh number Ra_m as a function of particle radius (or of relaxation time τ_v) is similar to the behavior of the minimum critical Grashof number in the problem of the stability of convective flow in a minimum containing an additive in a vertical layer. An increase in *r* leads to an increase in equilibrium stability up to some limiting value $r_* = 0.0045$ at which $Ra_m = 3139$. The stabilizing effect decreases when $r > r_*$. The critical wave number k_m increase in *r* and reaches a value of 3.19, and then decreases with further increase in *r*. In contrast to the problem of the stability of steady-state convective motion of containing additive, the increase in convective equilibrium stability with increase in particle size is associated with a decrease in the length of dangerous standing perturbations.

5. A comparison of these results with the results of [10] shows that settling particles produce a considerably greater stabilizing effect on steady-state flow of a fluid than suspended particles. In fact, neglect of particle settling rate in comparison with the velocity of steady-state flow of a fluid valid for sufficiently fine particles of not too great a density (with respect to the density of the transporting medium). Coarse dense particles are more inert than fine particles, and it is impossible to neglect their settling rate. The particle slip rate with respect to the fluid is of the order of the quantity u_s. The resultant relative motion of fluid and particles leads to additional dissipation of perturbation energy in comparison with the case of suspended particles.

REFERENCES

1. Gupalo Yu. P. "Stability of laminar flow of a liquid with heavy impurity," *Izv. Akad. Nauk SSSR, Otd. Tekh. Nauk, Mekh. Mashinostr*., 1960; No. 6, 38-46.

2 Saffman P. G. "On the stability of laminar flow of a dusty gas," *J. Fluid Mech*., 1962; 18, No. 1, 120-128.

3. Michael D. H. "The stability of plane Poiseuille flow of a dusty gas," *J. Fluid Mech.,* 1964; 18, No.1, 19-32.

4. Zheltukhin I. D. "Stability of a laminar boundary layer in an incompressible gas carrying a heavy impurity," *Izv. Akad. Nauk SSSR, Mekh. Zhidk. Gaza*, 1971; No.2, 103-110.

5. Gupalo Yu. P., Ryazantsev Yu. S., Sergeev Yu. A. "Convective instability of a homogeneous suspended layer," Izv. Akad. Nauk SSSR, Mekh. Zhidk. Gaza. 1982; No. 3, 112-114

6. Dement'ev, O. "Convective stability of a medium containing a heavy solid addutive". Zhurnal Prikladnoi Mekhaniki I Tekhnicheskoi Fiziki, No. 3. 1976, P. 105-115.

7. Marble F. E. "Dynamics of dusty gases," *Mekhanik,*. 1970; No. 6, 397-404.

8. Sow S. "Hydrodynamics of Multiphase Systems "[Russian translation], Mir, Moscow, 1971. P. 576.

9. Gershuni, G.Z., Zhukhovitskii E.M., Nepomnjashchy A.A. "Stability of convective flows". Moscow, Nauka. 1989, P. 320.

10. Dementiev O. "Stability of steady-state flows of a liquid with a heavy impurity", Z. angew. Math. und Mech., 1996; v. 5, 112-114.

3D electron beam distribution estimation by neural models

Elena Koleva[1,2*], Lilyana Koleva[2**], Tsvetomira Tsonevska[1]

Institute of Electronics, Bulgarian Academy of Sciences, Bulgaria[1]
University of Chemical Technology and Metallurgy, Bulgaria[2]

[*]eligeorg@abv.bg, [**]sura@abv.bg

Abstract: *The electron beam technological processes like electron beam welding, electron beam additive technologies, etc. depend strongly on the characteristics of the electron beam, generated by the electron gun. In this work the estimation of the 3D radial current density distribution using training, testing and validation of different artificial neural networks is considered. The model estimation is based on experimental measurements of the electron beam current distribution in three cross-sections of the beam at different distances from the magnetic lens of the electron gun. The estimated neural models with different structures are compared. Graphical user interface for the evaluation of the radial electron beam distribution in any cross-sections of the beam is developed.*

Keywords*: ELECTRON BEAM CURRENT DISTRIBUTION, GRAPHICAL USER INTERFACE, NEURAL NETWORK MODELS.*

1. Introduction

The electron beam technological processes like electron beam welding, electron beam additive technologies, etc. depend strongly on the characteristics of the electron beam, generated by the electron gun. The characterization of the electron beam is one of the necessary conditions for the transfer of technologies from one equipment to another, as well as for the comparison of the quality of different electron beam facilities (guns).

The knowledge of the radial current distribution in different beam cross-section planes is the first step in the electron beam characterization [1 - 3]. It helps the determination of the crossover (focus) position. Better understanding for the electron beam/work-piece interaction along the beam penetration depth and the ability for its prognostication are defined by the simultaneous evaluation of radial and angular distribution of the beam electrons. The electron beam emittance [4] is a suitable parameter for standardization of the electron optical technology systems, which can be calculated applying the estimated parameters of the radial and the angular distributions of the beam. The evaluation of this parameter is a key condition for achieving good quality, repeatability and reproducible performance of electron beam welds. The emittance strongly influences the ability of the electron beam to penetrate into the processed material and directly determines the maximal depth of the welded joints, obtained by electron beam welding. This parameter forms the basis for transferring a concrete technology from one machine to another which will minimize the volume of preliminary experimental tests to adjust the process parameters as well as will extend the capability of the expert systems to define the process parameter settings during welding (or other processing) of different materials.

In this work the estimation of the 3D radial current density distribution using training, testing and validation of different artificial neural networks is considered. The model estimation is based on experimental measurements of the electron beam current distribution in three cross-sections of the beam at different distances from the magnetic lens of the electron gun. The estimated neural models with different structures are compared. Graphical user interface for the evaluation of the radial electron beam distribution in different cross-sections of the beam is developed.

2. Experimental conditions

The electron beam spot is analyzed in three cross sections by implementation of the beam current point by point measurement in 100 points (10 × 10) in each cross-section. This number of points, if they are small enough, is sufficient to determine several peaks (three-dimensional formations in 3D current distribution diagrams (Fig. 1). The total measurement time of the selected number of tested points – 100 – is approximately equal to for 20 s and the total time to determine the value of current density at one point is 140 ms.

The procedure for measuring the current in a given position of the plates (*x*, *y*) is the following:

a) measuring the current collected by the Faraday cylinder; this happens in about 15 ms. During this time, this current is measured 10 - 30 times and its average value is calculated and stored in computer memory;

b) the electron beam is defocused and deflected on a powerful energy collector;

c) the analytical plate is moved to the next position. Eventually, the first protective plate is moved at the same time, if all measurements at a given position have been made;

d) the electron beam is returned to the measuring position at the focus at which the beam is examined. The time to establish the normal focus of the beam (and distribution in the steady beam) is of the order of 15 ms.

After that the measuring the current of the Faraday cylinder at the new position of the new point is repeated from point a).

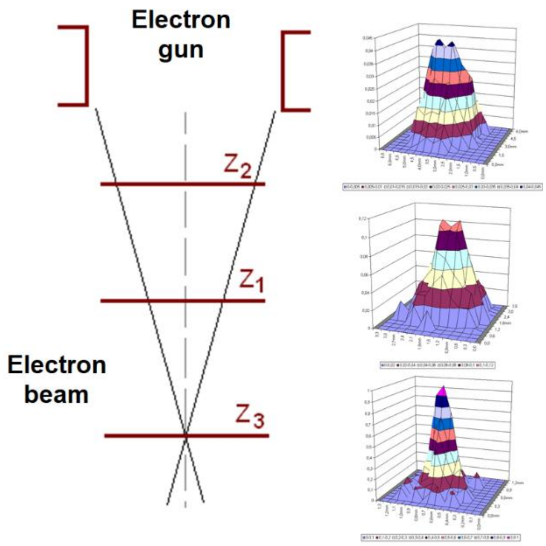

Fig. 1 *Measured electron beam current distributions in three cross-sections of the beam: z_1 = 245 mm, z_2 = 170 mm and z_3 = 320 mm from the end of the focusing coils of the electron gun.*

The data on the current density distributions *j*(*x*, *y*) are obtained in three beam sections at distances: z_1 = 245 mm, z_2 = 170 mm and z_3 = 320 mm from the end of the focus coils. The parameters of the electron beam are: beam power 2.4 kW, beam current 40 mA and accelerating voltage 60 kV. At a distance of z_3 = 320 mm is found the crossover of the electron beam.

3. Neural Networks

Neural networks (NN) are universal approximators with low sensitivity to errors, which determines the benefits of their use in different application areas [5, 6].

For developing an expert system for defining the electron beam current density distribution an input-output structure of the neural network-based model is used, i.e. the neural network consists of 3 input neurons, hidden layer (with different number of neurons), and 1 output neuron.

The methodology, implemented for developing of neural network models, consists of the following general steps:

- Selecting the type and structure of the NN model structure.
- Training of the created NN by using the back-propagation method experimentally obtained (and/or numerically simulated) set of training data to a satisfactory accuracy [5, 7, 8].
- Choosing the neural network model structure.
- Recall of the trained neural network for prediction, investigation and parameter optimization.

For comparison of the neural network models the mean squared error (MSE) (1), as well as the regression multiple correlation coefficient R (2) are calculated:

$$MSE = \frac{\sum_{i=1}^{n}(\hat{y}_i - y_i)^2}{n}, \tag{1}$$

$$R = \sqrt{1 - \frac{\sum_{i=1}^{n}(y_i - \hat{y}_i)^2}{\sum_{i=1}^{n}(y_i - \bar{\bar{y}})^2}}, \tag{2}$$

where $\hat{y}$ and y is the predicted and the experimental values, $\bar{\bar{y}}$ is the overall average of all mean values, and n is the number of data.

For training, validation and testing of the neural networks, the experimental data are randomly separated into 3 parts: 70 % (506 datasets) for training, 15 % (108 datasets) for validation and 15 % (108 datasets) for testing.

3.1. Feedforward neural network

Feedforward neural network consists of a series of layers. The first layer has a connection from the network input. Each subsequent layer has a connection from the previous layer. The final layer produces the network's output.

Feedforward networks can be used for any kind of inputs to output mapping. A feedforward network with one hidden layer and enough neurons in the hidden layers can fit any finite input-output mapping problem. Two-layer feed-forward network with sigmoid hidden neurons and linear output neurons is presented in Fig. 2. The network is trained with Levenberg-Marquardt backpropagation algorithm [6, 8].

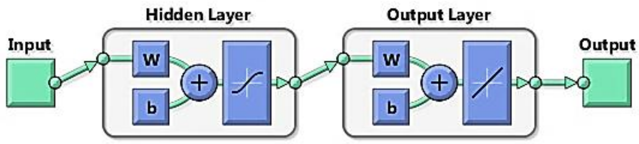

Fig. 2 *Feedforward neural network structure*

Matlab environment is used to implement the described approach for training NN with different structures of the hidden layer – with 3, 5, 10 and 15 hidden units and different random sets for training (506 datasets), for validation (108 datasets) and for testing (108 datasets). The best four Neural network models, based on the experimental observations are chosen.

The obtained results for the accuracy of the training, validation and testing of these four NN models are presented in Table 1 – Table 3 correspondently.

Table 1. *Feedforward neural network training results*

	NN with 3 hidden neurons	*NN with 5 hidden neurons*	*NN with 10 hidden neurons*	*NN with 15 hidden neurons*
MSE	0.007784	0.003978	0.001244	0.002359
R	0.5245	0.683	0.8182	0.8595

Table 2. *Feedforward neural network validation results*

	NN with 3 hidden neurons	*NN with 5 hidden neurons*	*NN with 10 hidden neurons*	*NN with 15 hidden neurons*
MSE	0.001902	0.0104	0.004465	0.004205
R	0.6927	0.6449	0.7561	0.8708

Table 3. *Feedforward neural network testing results*

	NN with 3 hidden neurons	*NN with 5 hidden neurons*	*NN with 10 hidden neurons*	*NN with 15 hidden neurons*
MSE	0.00611	0.00456	0.01616	0.002229
R	0.6165	0.7704	0.8719	0.8198

From the tables it can be seen, that from these four structures better results are obtained by using the neuron network models with a hidden layer, consisting from 15 hidden neurons, due to the smaller values of MSE and closer to 1 values of the coefficient R, obtained during training, validation and testing stages.

The NN whit 15 hidden neurons training, validation and testing results from accuracy cross-validations for the electron beam current distribution estimation are presented in Fig. 3.

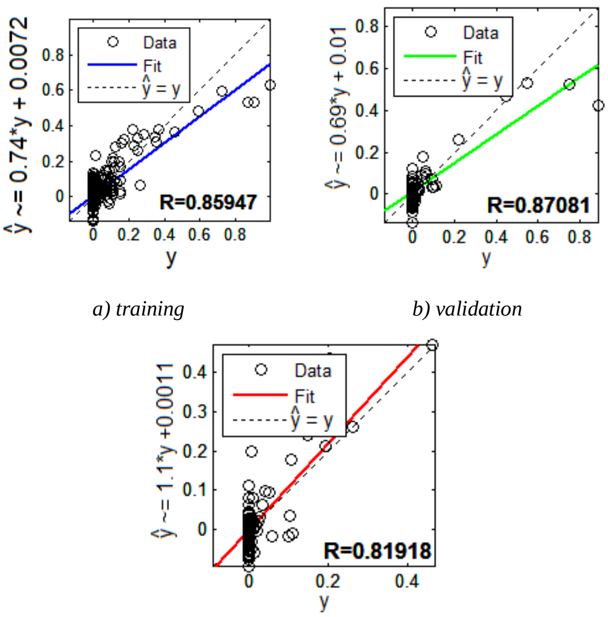

a) training *b) validation*

c) testing

Fig. 3 *Feedforward neural network whit 15 hidden neurons: a) training, b) validation and c) testing results for defining the electron beam current density distribution.*

4. Expert System

Matlab environment is used to develop a Graphical user interface (GUI), shown in Fig. 4, which represents a part of an expert system for decision making for the management and control of the electron beam.

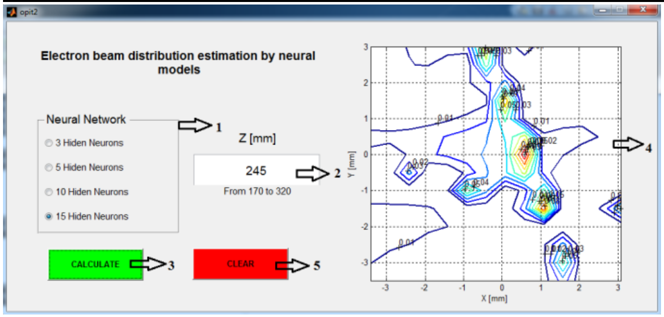

Fig. 4 *Graphical user interface for 3D electron beam distribution estimation.*

In Fig. 4 it can be seen that the developed Graphical user interface for 3D electron beam radial current distribution estimation has a radio-button section "1" for the choice of the structure of the Neural network model with several options for the user:

- Neural Network with 3 hidden neurons;
- Neural Network with 5 hidden neurons;
- Neural Network with 10 hidden neurons;
- Neural Network with 15 hidden neurons.

Once the desired structure of the neural model has been selected, a value must be entered in field "2", within the limits indicated below the field (from 170 to 320 mm) for the distance of the beam cross-section from the end of the focusing coils of the electron gun.

By pressing the "Calculate" button "3", the necessary calculations are initialized with the selected neural network model "1" and the value entered in field "2".

Prior to the calculation for the estimation of the electron beam current distribution, the expert system checks whether the input parameter "2" is correct and whether it falls within the specified limits. If the check concludes that the entered value is incorrect, a message in the field "4" inviting the user to enter a valid value (Fig. 5) is displayed. If the input value passes the check and it is in considered region, the calculation continues with the chosen neural network model and result is graphical presentation of the contour plot, shown in field "4".

There is a function in Fig. 4 presented by button "5" or "Clear". Pressing this button, the program clears all data from fields "2" and "4" and the expert system is ready for the next calculation.

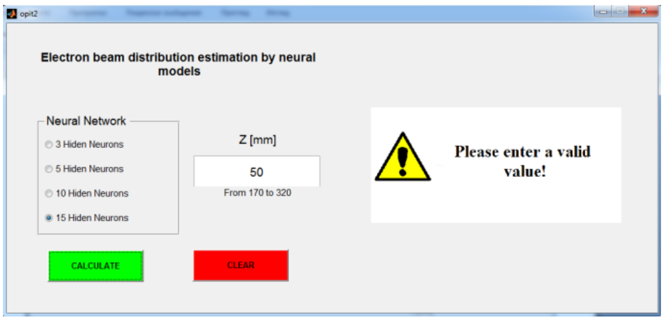

Fig. 5 *Error message for the incorrect input value.*

5. Conclusions

In this work presents the results from the estimation of the 3D radial current density distribution using training, testing and validation of different artificial neural networks. The model estimation is based on experimental measurements of the electron beam current distribution in three cross-sections of the beam at different distances from the magnetic lens of the electron gun. The estimated neural models with different structures are compared. Matlab environment is used to develop a Graphical user interface (GUI) for 3D radial current density distribution calculation, which represents a part of an expert system for decision making for the management and control of the electron beam.

Acknowledgements

The research was conducted within the framework of the project KP-06-N27/18, funded by the National Fund "Scientific Investigations", and of the National Science Program "Information and Communication Technologies for a Digital Single Market in Science, Education and Security (ICTinSES)", funded by the Ministry of Education and Science.

References

1. G. Mladenov, E. Koleva, *Design of High Brightness Welding Electron Guns and Characterization of Intense Electron Beam Quality*, (Welding: Processes, Quality, and applications, Ed. Richard J. Klein, Nova Sci. Publishers, SeriaMechanical Engineering-Theory and Applications, 1761-320-3, 2010)
2. E. Koleva, G. Mladenov, M. Kardjiev, D. Todorov, Elektrotechnica & Elektronica - E+E, **49**(5-6), 46-55 (2014)
3. E. Koleva, L. Koleva, D. Todorov, G. Mladenov, J. of Phys. Conf. Ser., **700**, 012013 (2016)
4. E. Koleva, G. Mladenov, V. Dzharov, D. Todotov, M. Kerdjiev, L. Koleva, Electrotechnica & Electronica – E+E, **51**(5-6), 184 – 188 (2016)
5. E. Koleva, N. Christova, K. Velev. Proc. of Int. conf. IEEE Intell. Syst. (London, UK), 7-9 (2010)
6. E. Koleva, N. Christova, G. Mladenov, D. Trushnikov, V. Belenkiy, Proc. Conf. "Electonica 2014", 120-128 (2014)
7. K. Hornik, M. Stinchcombe, H. White, Neural Nets., **2**(5), 359 – 366 (1989)
8. H. Tang, K.C. Tan, Z. Yi, *Neural Networks: Computational Models and Applications* (Springer, 2007).

Comparison of three methods for the pump energy analysis

Mrzljak Vedran, Lorencin Ivan, Anđelić Nikola, Baressi Šegota Sandi
Faculty of Engineering, University of Rijeka, Vukovarska 58, 51000 Rijeka, Croatia
E-mail: vedran.mrzljak@riteh.hr, ilorencin@riteh.hr, nandelic@riteh.hr, sbaressisegota@riteh.hr

Abstract: *This paper presents a comparison of three methods for any pump energy analysis. Each method is used for the analysis of three different water pumps from the conventional steam thermal power plant – two feed water pumps (FWP1 and FWP2) and condensate pump (CP). For each pump three essential types of mechanical power which defines all energy analysis methods are: delivered power from power producer, real (polytropic) power and ideal (isentropic) power. Method 1 which compares delivered and real (polytropic) power show the best performances, while Method 3 which compare delivered and ideal (isentropic) power should be avoided because it results with too high energy power loss and too low energy efficiency of any pump. Method 2 which compares real (polytropic) and ideal (isentropic) pump power can be used as a good compromise for the pump energy analysis in the most of the cases – its results are similar to results of Method 1.*
KEYWORDS*: PUMP, VARIOUS ENERGY ANALYSIS METHODS, ENERGY LOSS, ENERGY EFFICIENCY*

1. Introduction

Pumps are unavoidable components of various steam power plants [1-3], combined-cycle power plants [4, 5], cogeneration plants [6] and many different power and energy systems [7, 8].

The pumps function is the same as a function of compressors or turbocompressors – increasing of operating medium pressure [9, 10]. The only difference between pumps and compressors is in operating medium – pumps operate with liquids, while compressors and turbocompressors operate with gases, vapors and its mixtures [11, 12].

In the literature can be found pumps of various types which operate in different operating regimes [13]. Regardless of pump type or operating regime, the crucial element in energy analysis of any pump is taking into account three types of mechanical power which defines various losses – delivered mechanical power to pump from the mechanical power producer, mechanical power required for real (polytropic) pressure increase of liquid and mechanical power required for ideal (isentropic) liquid pressure increase.

The comparison of the mentioned types of mechanical power defines all the methods for any pump energy analysis. In this paper is described and presented each energy analysis method for any pump and all the methods are compared at each of three pumps from the conventional steam thermal power plant. Those pumps are two feed water pumps (FWP1 and FWP2) as well as condensate pump (CP). For each observed pump are calculated energy power losses and energy efficiencies by using each of three energy analysis methods. The obtained results are discussed in detail.

2. Pump description and operating characteristics

As the analysis in this paper will be performed by using three water pumps, all of the descriptions and explanations are based on the water as the operating medium for the pump (again, it must be taken into account that operating medium can be any liquid).

Operation principle of any pump is presented in Fig. 1. The pump takes liquid (water) of a lower pressure, increases its pressure and delivers liquid with a higher pressure to a higher pressure component [14]. For the liquid pressure increase, any pump uses mechanical power delivered from the mechanical power producer which are in the most of the cases electrical motors or in some situations steam or gas low-power turbines [15-17]. Mechanical power delivered to pump from mechanical power producer is the highest mechanical power related to any pump – it takes into account all the losses in shafts, bearings, pump inner losses and all the other losses which occur in power distribution.

For proper pump energy analysis (regardless of used method) are required operating parameters of liquid at pump suction side (inlet) and at the pump compression side (outlet). Those liquid operating parameters at the pump inlet and outlet are liquid pressure, temperature and mass flow rate. Therefore, pump operation can be analyzed only by measuring described liquid operating parameters at both sides of any pump. In Fig. 1, the operating points in which the measurements should be obtained are marked with yellow dots and marked as water inlet (input) and water outlet (output).

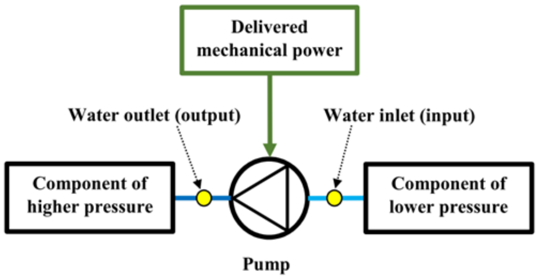

Fig. 1. *Scheme of the pump with two operating points (marked yellow) required for the analysis*

Measured operating parameters of liquid at the pump inlet (input) and at the pump outlet (output) defines real (polytropic) process of a pump, Fig. 2. This process takes into account all the losses which occur during liquid pressure increase. Losses during liquid pressure increase can be seen in liquid specific entropy increase at the pump outlet (in comparison to pump inlet). Second mechanical power related to any pump is real (polytropic) power, which is required for real (polytropic) pressure increase process. From the measured liquid operating parameters at the pump inlet and outlet can be calculated mechanical power required for the real (polytropic) process.

The third and final mechanical power of any pump is ideal (isentropic) mechanical power. This power can also be calculated from the measured liquid operating parameters at the pump inlet and from the calculated liquid operating parameters at the pump outlet. In ideal (isentropic) pump process, liquid operating parameters at the pump inlet are the same as in the real (polytropic) process. However, the difference in ideal and real pump pressure increase process can be seen in liquid operating parameters at the pump outlet. Ideal (isentropic) pressure increase process is a process between the same pressures but with assuming always the same liquid specific entropy, Fig. 2. Always the same liquid specific entropy during the pressure increase neglected any losses during such process. Any real process should be as close as possible to the ideal one, but due to losses, real process will never achieve the ideal one. By knowing the liquid specific entropy and pressure at the pump outlet can be calculated all the other liquid operating parameters in ideal process and therefore, from those parameters can be calculated ideal (isentropic) mechanical power.

Comparison of pump ideal and real pressure increase process, Fig. 2, leads to conclusion that in the real process pump will require more mechanical power (due to higher difference in liquid specific enthalpies at pump outlet and inlet). In both real and ideal pump processes, liquid mass flow rate is the same. As any pump is a mechanical power consumer, in ideal (isentropic) pressure increase process, between the same pressures as in the real process, pump will require the lowest mechanical power (in comparison to real and delivered mechanical power). From this point of view, for any pump is always valid following mechanical power relation:

$$P_{\text{delivered}} > P_{\text{real (polytropic)}} > P_{\text{ideal (isentropic)}}, \tag{1}$$

where P is mechanical power in (kW).

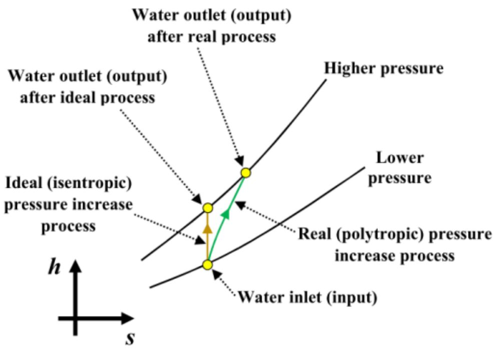

Fig. 2. *A comparison of real (polytropic) and ideal (isentropic) liquid pressure increase process in specific enthalpy-specific entropy diagram*

3. Equations for the energy analysis

3.1. General energy analysis equations and balances

The first law of thermodynamics defines energy analysis of any system or a control volume [18, 19]. The general energy balance equation, disregarding potential and kinetic energies, is [20]:

$$\dot{Q}_{\text{in}} + P_{\text{in}} + \sum \dot{E}n_{\text{in}} = \dot{Q}_{\text{out}} + P_{\text{out}} + \sum \dot{E}n_{\text{out}}, \tag{2}$$

where $\dot{Q}$ in (kW) is energy heat transfer, index in is related to the inlet (input) and index out is related to the outlet (output). $\dot{E}n$ is a total energy of operating medium flow in (kW) [21], defined by the equation:

$$\dot{E}n = \dot{m} \cdot h, \tag{3}$$

where $\dot{m}$ is operating medium mass flow rate in (kg/s) and h is operating medium specific enthalpy in (kJ/kg). Overall definition of the energy efficiency of any system or a control volume is [22, 23]:

$$\eta_{\text{en}} = \frac{\text{cumulative energy outlet (output)}}{\text{cumulative energy inlet (input)}}. \tag{4}$$

During the energy analysis of any system or a component usually did not occur any operating medium mass flow rate leakage, therefore it is also valid following mass flow rate balance [24]:

$$\sum \dot{m}_{\text{in}} = \sum \dot{m}_{\text{out}}. \tag{5}$$

All the general energy analysis equations and balances will be used in the following equations of three pump energy analysis methods.

3.2. Equations for three energy analysis methods of the pump

All pump energy analysis methods are based on the principles and operating parameters presented in Fig. 1 and Fig. 2. It should be noted that in any method must be fulfilled pump mechanical power relation presented in Eq. 1.

Method 1

The first method of pump energy analysis is based on comparison of mechanical power delivered to pump from power producer and real (polytropic) power required for real pump pressure increase process. The main problem of this method in practical calculations is that for many pumps, mechanical power delivered from mechanical power producer is not known or measured [25] because in each complex process pumps are auxiliary devices. Equations for this method will be derived from [26].

Pump energy power loss by using this method is:

$$\dot{E}n_{\text{PL,M1}} = \dot{m}_{\text{in}} \cdot h_{\text{in}} + P_{\text{delivered}} - \dot{m}_{\text{out}} \cdot h_{\text{out}}, \tag{6}$$

where mechanical power delivered from mechanical power producer is measured variable. Mechanical power for the real (polytropic) pump pressure increase process is derived from measured fluid operating parameters at the pump inlet and outlet:

$$P_{\text{real (polytropic)}} = \dot{m}_{\text{out}} \cdot h_{\text{out}} - \dot{m}_{\text{in}} \cdot h_{\text{in}}, \tag{7}$$

therefore, pump energy power loss by using this method can be presented as:

$$\dot{E}n_{\text{PL,M1}} = P_{\text{delivered}} - P_{\text{real (polytropic)}}. \tag{8}$$

Pump energy efficiency by using this method is:

$$\eta_{\text{en,M1}} = \frac{\dot{m}_{\text{out}} \cdot h_{\text{out}} - \dot{m}_{\text{in}} \cdot h_{\text{in}}}{P_{\text{delivered}}} = \frac{P_{\text{real (polytropic)}}}{P_{\text{delivered}}}. \tag{9}$$

Method 2

A second method of pump energy analysis is based on comparison of mechanical power which pump use in real (polytropic) pressure increase process and mechanical power which pump will use in ideal (isentropic) pressure increase process. This is the most common used method due to the highest data availability. This method, in fact, compared real pump process with the process which can be obtained in ideal situation.

Mechanical power for the ideal (isentropic) pump pressure increase process is:

$$P_{\text{ideal (isentropic)}} = \dot{m}_{\text{out}} \cdot h_{\text{out,IS}} - \dot{m}_{\text{in}} \cdot h_{\text{in}}, \tag{10}$$

where index IS denotes isentropic process. Mechanical power for the pump real (polytropic) pressure increase process is calculated by using Eq. 7. Pump energy power loss by using this method is:

$$\dot{E}n_{\text{PL,M2}} = P_{\text{real (polytropic)}} - P_{\text{ideal (isentropic)}}. \tag{11}$$

Pump energy efficiency by using this method is:

$$\eta_{\text{en,M2}} = \frac{P_{\text{ideal (isentropic)}}}{P_{\text{real (polytropic)}}}. \tag{12}$$

Method 3

The third method of pump energy analysis is based on comparison of delivered mechanical power from mechanical power producer and mechanical power which pump will use in the ideal (isentropic) pressure increase process. Delivered mechanical power from mechanical power producer is measured inside the power plant, while the mechanical power for the ideal (isentropic) pump pressure increase process is calculated by using Eq. 10.

Pump energy power loss by using this method is:

$$\dot{E}n_{\text{PL,M3}} = P_{\text{delivered}} - P_{\text{ideal (isentropic)}}. \tag{13}$$

Pump energy efficiency by using this method is:

$$\eta_{\text{en,M3}} = \frac{P_{\text{ideal (isentropic)}}}{P_{\text{delivered}}}. \tag{14}$$

4. Water operating parameters at pump input (inlet) and output (outlet) required for the analysis

Three described pump energy analysis methods are compared at each of three water pumps which required operating parameters are found in the literature [27].

Required water operating parameters (pressure, temperature and mass flow rate) at each pump inlet and outlet are presented in Table 1. Observed pumps are two feed water pumps (FWP1 and FWP2) as well as condensate pump (CP).

Table 1. *Water operating parameters at input (inlet) and output (outlet) of each pump [27]*

Pump	Operating point	Water mass flow rate (kg/s)	Water temperature (K)	Water pressure (kPa)
FWP1	Inlet	59.27	452.55	1032
	Outlet	59.27	456.34	18355
FWP2	Inlet	59.98	452.55	1030
	Outlet	59.98	456.34	18359
CP	Inlet	89.91	315.12	35.28
	Outlet	89.91	316.23	1618

By using water pressure and temperature at the inlet and outlet of each pump are calculated water specific enthalpies and specific entropies by using NIST REFPROP 9.0 software [28] and presented in Table 2. Required water specific enthalpies and specific entropies are calculated for both real (polytropic) as well as for the ideal (isentropic) water pressure increase process for each pump. From Table 2 can be seen that in the ideal (isentropic) pressure increase process water specific entropy at the inlet and outlet of each pump remains the same.

Table 2. *Water specific enthalpies and specific entropies at input (inlet) and output (outlet) of each observed pump in real (polytropic) and ideal (isentropic) pressure increase processes*

Pump	Operating point	Water specific enthalpy – real (polytropic) process (kJ/kg)	Water specific entropy – real (polytropic) process (kJ/kg·K)	Water specific entropy – ideal (isentropic) process (kJ/kg·K)	Water specific enthalpy – ideal (isentropic) process (kJ/kg)
FWP1	Inlet	760.43	2.1334	2.1334	760.43
	Outlet	785.97	2.1468	2.1334	779.86
FWP2	Inlet	760.43	2.1334	2.1334	760.43
	Outlet	785.97	2.1468	2.1334	779.86
CP	Inlet	175.79	0.5986	0.5986	175.79
	Outlet	181.82	0.6127	0.5986	177.39

5. Results and discussion

Energy power of water, calculated for each pump at inlet (input) and outlet (output) by using Eq. 3 is presented in Fig. 3. It can clearly be seen that both feed water pumps (FWP1 and FWP2) have much higher energy power inputs and outputs in comparison to condensate pump (CP).

It should be noted that FWP1 and FWP2 operates with much higher water pressures at inlet and outlet (Table 1) in comparison to CP, which is used for the pressure increase of condensate obtained in power plant main steam condenser.

The difference between energy power of water at each pump outlet and inlet denotes required mechanical power used in each pump (regardless of mechanical power type). Therefore, FWP2 will use the highest mechanical power, followed by FWP1, while the CP will use mechanical power much lower in comparison to both feed water pumps.

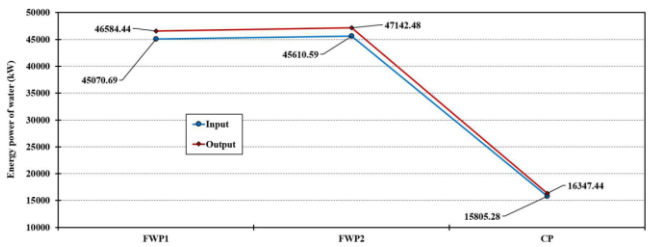

Fig. 3. *Comparison of water energy power input and output for three observed pumps*

The mechanical power relation for each pump, presented in Eq. 1 is clearly visible in Fig. 4. For each of three observed pumps delivered mechanical power is the highest one, followed by real (polytropic) power, while the lowest mechanical power is ideal (isentropic) one.

The conclusion obtained from Fig. 3 is also visible in Fig. 4 – FWP2 uses the highest mechanical power in comparison to other observed water pumps (regardless of the fact is that power delivered, real or ideal). Delivered mechanical power to FWP1, FWP2 and CP is equal to 1830 kW, 1860 kW and 850 kW, real (polytropic) power is equal to 1513.76 kW, 1531.89 kW and 542.16 kW, while ideal (isentropic) power is equal to 1151.62 kW, 1165.41 kW and 143.86 kW, respectively.

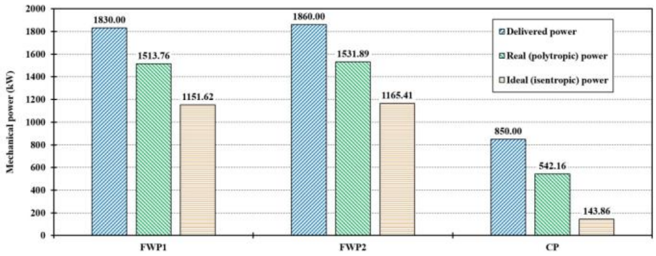

Fig. 4. *Comparison of delivered, real (polytropic) and ideal (isentropic) mechanical power for three observed water pumps*

Comparison of three methods for the pump energy analysis shows the same trends in energy power loss for each of three observed pumps, Fig. 5. The lowest energy power loss of each pump is obtained by using Method 1 (comparison of delivered and real power), followed by Method 2 (comparison of real and ideal power). It can be observed that Method 1 and Method 2 gives similar energy power loss for both feed water pumps, while the notable difference between those two methods in energy power loss can be seen only for condensate pump. Method 3 gives much higher energy power loss of each observed pump in comparison to the other two methods.

When comparing energy power loss trends between observed pumps, it can be seen that in Method 1 FWP2 has the highest, while CP has the lowest energy power loss, Fig. 5. Using Method 2 and Method 3 results with same trends in energy power loss – FWP1 has the lowest, while CP has the highest energy power loss.

A detail analysis and possible optimization of each of three observed pumps will be performed by using various artificial intelligence approaches [29-32].

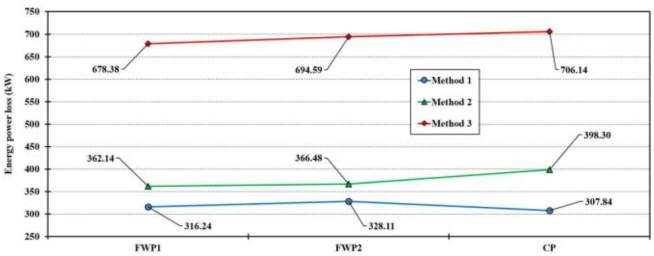

Fig. 5. *Energy power loss obtained in all energy analysis methods for three observed water pumps*

Comparison of Fig. 5 and Fig. 6 proves the fact that all of the observed pumps are components for which energy power loss and energy efficiency are reverse proportional.

Therefore, the highest energy efficiency of each observed pump will be obtained by using Method 1, while the lowest energy efficiency of each pump will be obtained by using Method 3.

Obtained energy efficiency for FWP1, FWP2 and CP is equal to 82.72%, 82.36% and 63.78% by using Method 1; 76.08%, 76.08% and 26.53% by using Method 2 and 62.93%, 62.66% and 16.92% by using Method 3, respectively, Fig. 6. Again, for both feed water pumps obtained energy efficiencies by using Method 1 and Method 2 are similar, while for the CP used energy analysis methods gives quite different results. For the CP, only Method 1 gives an acceptable energy efficiency result, while Method 2 and Method 3 gives unacceptably low energy efficiencies.

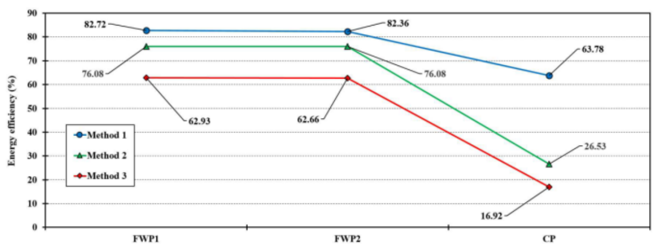

Fig. 6. *Energy efficiency obtained in all energy analysis methods for three observed water pumps*

Comparison in energy efficiency between all of the observed pumps gives as a result that the highest energy efficiency has FWP1, while the lowest energy efficiency has CP, regardless of used energy analysis method.

6. Conclusions

In this paper are presented three methods for any pump energy analysis. Each of observed methods is used for the analysis of three different water pumps from the conventional steam thermal power plant – two feed water pumps (FWP1 and FWP2) and condensate pump (CP). The most important conclusions are:

- The best energy analysis method for any pump is Method 1 which compare delivered and real (polytropic) mechanical power.
- Due to insufficient data (due to unknown delivered mechanical power from the mechanical power producer), Method 2 which compare real (polytropic) and ideal (isentropic) pump power can be used as a good compromise for the pump energy analysis – in the most of the cases obtained energy power loss and energy efficiency will be similar as in Method 1.
- The usage of Method 2 in the pump energy analysis can be questionable for the pumps which operate with low liquid pressure at the suction side.
- In any case, Method 3 should be avoided for the pump energy analysis, because it results with too high energy power loss and too low energy efficiency of any pump.

7. Acknowledgment

This research has been supported by the Croatian Science Foundation under the project IP-2018-01-3739, CEEPUS network CIII-HR-0108, European Regional Development Fund under the grant KK.01.1.1.01.0009 (DATACROSS), project CEKOM under the grant KK.01.2.2.03.0004, CEI project "COVIDAi" (305.6019-20), University of Rijeka scientific grant uniri-tehnic-18-275-1447, University of Rijeka scientific grant uniri-tehnic-18-18-1146 and University of Rijeka scientific grant uniri-tehnic-18-14.

8. References

[1] Ahmadi, G. R., Toghraie, D.: *Energy and exergy analysis of Montazeri steam power plant in Iran*, Renewable and Sustainable Energy Reviews 56, p. 454–463, 2016. (doi:10.1016/j.rser.2015.11.074)

[2] Mrzljak, V., Poljak, I.: *Energy analysis of main propulsion steam turbine from conventional LNG carrier at three different loads*, International Journal of Maritime Science & Technology "Our Sea" 66 (1), p. 10-18, 2019. (doi:10.17818/NM/2019/1.2)

[3] Naserbegi, A., Aghaie, M., Minuchehr, A., Alahyarizadeh, Gh.: *A novel exergy optimization of Bushehr nuclear power plant by gravitational search algorithm (GSA)*, Energy 148, p. 373-385, 2018. (doi:10.1016/j.energy.2018.01.119)

[4] Lorencin, I., Anđelić, N., Mrzljak, V., Car, Z.: *Genetic algorithm approach to design of multi-layer perceptron for combined cycle power plant electrical power output estimation*, Energies 12 (22), 4352, 2019. (doi:10.3390/en12224352)

[5] Adibhatla, S., Kaushik, S. C.: *Energy, exergy and economic (3E) analysis of integrated solar direct steam generation combined cycle power plant*, Sustainable Energy Technologies and Assessments 20, p. 88–97, 2017. (doi:10.1016/j.seta.2017.01.002)

[6] Burin, E. K., Vogel, T., Multhaupt, S., Thelen, A., Oeljeklaus, G., Gorner, K., Bazzo, E.: *Thermodynamic and economic evaluation of a solar aided sugarcane bagasse cogeneration power plant*, Energy 117, Part 2, p. 416-428, 2016. (doi:10.1016/j.energy.2016.06.071)

[7] Catrini, P., Cipollina, A., Micale, G., Piacentino, A., Tamburini, A.: *Exergy analysis and thermoeconomic cost accounting of a combined heat and power steam cycle integrated with a multi effect distillation-thermal vapour compression desalination plant*, Energy Conversion and Management 149, p. 950-965, 2017. (doi:10.1016/j.enconman.2017.04.032)

[8] Hafdhi, F., Khir, T., Ben Yahyia, A., Ben Brahim, A.: *Energetic and exergetic analysis of a steam turbine power plant in an existing phosphoric acid factory*, Energy Conversion and Management 106, p. 1230–1241, 2015. (doi:10.1016/j.enconman.2015.10.044)

[9] Sutton, I.: *Plant design and operations*, Elsevier Inc., 2015.

[10] Lorencin, I., Anđelić, N., Mrzljak, V., Car, Z.: *Multilayer Perceptron approach to Condition-Based Maintenance of Marine CODLAG Propulsion System Components*, Scientific Journal of Maritime Research 33 (2), p. 181-190, 2019. (doi:10.31217/p.33.2.8)

[11] Koroglu, T., Sogut, O.S.: *Conventional and advanced exergy analyses of a marine steam power plant*, Energy 163, p. 392-403, 2018. (doi:10.1016/j.energy.2018.08.119)

[12] Mrzljak, V., Anđelić, N., Lorencin, I., Car, Z.: *Analysis of gas turbine operation before and after major maintenance*, Journal of Maritime & Transportation Sciences 57 (1), p. 57-70, 2019. (doi:10.18048/2019.57.04)

[13] Mrzljak, V., Prpić-Oršić, J., Poljak, I.: *Energy power losses and efficiency of low power steam turbine for the main feed water pump drive in the marine steam propulsion system*, Journal of Maritime & Transportation Sciences 54 (1), p. 37-51, 2018. (doi:10.18048/2018.54.03)

[14] Moran M., Shapiro H., Boettner, D. D., Bailey, M. B.: *Fundamentals of engineering thermodynamics*, 7th edition, John Wiley and Sons, Inc., 2011.

[15] Kostyuk, A., Frolov, V.: *Steam and gas turbines*, Mir Publishers, Moscow, 1988.

[16] Mrzljak, V., Poljak, I., Mrakovčić, T.: *Energy and exergy analysis of the turbo-generators and steam turbine for the main feed water pump drive on LNG carrier*, Energy Conversion and Management 140, p. 307–323, 2017. (doi:10.1016/j.enconman.2017.03.007)

[17] Mrzljak, V.: *Low power steam turbine energy efficiency and losses during the developed power variation*, Technical Journal 12 (3), p. 174-180, 2018. (doi:10.31803/tg-20180201002943)

[18] Kanoğlu, M., Çengel, Y.A., Dincer, I.: *Efficiency evaluation of energy systems*, Springer Briefs in Energy, Springer, 2012.

[19] Kocijel, L., Poljak, I., Mrzljak, V., Car, Z.: *Energy Loss Analysis at the Gland Seals of a Marine Turbo-Generator Steam Turbine*, Technical Journal 14 (1), p. 19-26, 2020. (doi:10.31803/tg-20191031094436)

[20] Medica-Viola, V., Baressi Šegota, S., Mrzljak, V., Štifanić, D.: *Comparison of conventional and heat balance based energy analyses of steam turbine*, Scientific Journal of Maritime Research 34 (1), p. 74-85, 2020. (doi:10.31217/p.34.1.9)

[21] Medica-Viola, V., Mrzljak, V., Anđelić, N., Jelić, M.: *Analysis of Low-Power Steam Turbine With One Extraction for Marine Applications*, International Journal of Maritime Science & Technology "Our Sea" 67 (2), p. 87-95, 2020. (doi:10.17818/NM/2020/2.1)

[22] Mrzljak, V., Blecich, P., Anđelić, N., Lorencin, I.: *Energy and exergy analyses of forced draft fan for marine steam propulsion system during load change*, Journal of Marine Science and Engineering 7 (11), 381, 2019. (doi:10.3390/jmse7110381)

[23] Taheri, M. H., Mosaffa, A. H., Garousi Farshi, L.: *Energy, exergy and economic assessments of a novel integrated biomass based multigeneration energy system with hydrogen production and LNG regasification cycle*, Energy 125, p. 162-177, 2017. (doi:10.1016/j.energy.2017.02.124)

[24] Lorencin, I., Anđelić, N., Mrzljak, V., Car, Z.: *Exergy analysis of marine steam turbine labyrinth (gland) seals*, Scientific Journal of Maritime Research 33 (1), p. 76-83, 2019. (doi:10.31217/p.33.1.8)

[25] Noroozian, A., Mohammadi, A., Bidi, M., Ahmadi, M. H.: *Energy, exergy and economic analyses of a novel system to recover waste heat and water in steam power plants*, Energy Conversion and Management 144, p. 351–360, 2017. (doi:10.1016/j.enconman.2017.04.067)

[26] Mrzljak, V., Žarković, B., Poljak, I.: *Energy and exergy analysis of sea water pump for the main condenser cooling in the LNG carrier steam propulsion system*, Proceedings of International scientific conference Mathematical Modeling 2017, p. 92-95, Borovets, Bulgaria, 2017.

[27] Uysal, C., Kurt, H., Kwak H.-Y.: *Exergetic and thermoeconomic analyses of a coal-fired power plant*, International Journal of Thermal Sciences 117, p. 106-120, 2017. (doi:10.1016/j.ijthermalsci.2017.03.010)

[28] Lemmon, E.W., Huber, M.L., McLinden, M.O.: *NIST reference fluid thermodynamic and transport properties - REFPROP*, version 9.0, User's guide, Colorado, 2010.

[29] Lorencin, I., Anđelić, N., Mrzljak, V., Car, Z.: *Marine objects recognition using convolutional neural networks*, International Journal of Maritime Science & Technology "Our Sea" 66 (3), p. 112-119, 2019. (doi:10.17818/NM/2019/3.3)

[30] Car, Z., Baressi Šegota, S., Anđelić, N., Lorencin, I., Mrzljak, V.: *Modeling the Spread of COVID-19 Infection Using a Multilayer Perceptron*, Computational and Mathematical Methods in Medicine, 2020. (doi:10.1155/2020/5714714)

[31] Lorencin, I., Anđelić, N., Španjol, J., Car, Z.: *Using multi-layer perceptron with Laplacian edge detector for bladder cancer diagnosis*, Artificial Intelligence in Medicine, 102, 101746, 2020. (doi:10.1016/j.artmed.2019.101746)

[32] Baressi Šegota, S., Lorencin, I., Ohkura, K., Car, Z.: *On the traveling salesman problem in nautical environments: an evolutionary computing approach to optimization of tourist route paths in Medulin, Croatia*, Journal of Maritime & Transportation Sciences 57 (1), p. 71-87, 2019. (doi:10.18048/2019.57.05)

Linear synthesis of frame eddy current probes with a planar excitation system

Trembovetska R., PhD Eng., Assoc. Prof .; Halchenko V.Ya., Dr.Sc. Eng., Prof .; Tychkov V., PhD Eng., Assoc. Prof.; Bazilo C.V., Dr.Sc. Eng., Assoc. Prof.
Faculty of Electronic Technologies and Robotics – Cherkasy State Technological University, Ukraine

r.trembovetska@chdtu.edu.ua

Abstract: *A mathematical method of linear surrogate parametric synthesis of frame surface non-coaxial eddy current probes with a uniform eddy current density distribution in the testing object's zone is proposed. The metamodel of a frame eddy current probe with a planar structure of the excitation system is constructed. Acceptable accuracy of the created metamodel is obtained by using the decomposition of the extremum search space and using associative neural networks. Examples of the synthesis of such excitation systems using modern metaheuristic stochastic algorithms for finding the global extremum are considered. The numerical results of the obtained solution and graphic illustrative material of the density distribution of the eddy currents on the surface in the testing object's zone are given.*

Keywords*: FRAME EDDY CURRENT PROBE, PLANAR STRUCTURE OF THE EXCITATION SYSTEM, EDDY CURRENTS DENSITY, UNIFORM SENSITIVITY, NEURAL NETWORKS*

1. Introduction

Creation of favorable conditions for reliable detection of defects and determination of their geometrical parameters by means of eddy current testing is an urgent and at the same time complex problem. A wide range of scientists is engaged in research on the problem of creating a homogeneous and tangential field of probes excitation. The authors propose the creation of electromagnetic field (EMF) with a predetermined topology, which makes it possible to improve the selectivity and sensitivity of surface eddy current probes (SECP) [1-5]. The solutions usually proposed by them on the a priori given properties of the EMF are based on the creation of an uneven distribution of the excitation current in the generator coil of the SECP or on the use of a special geometry of the excitation winding. A detailed review of scientific and technical information on the use of EMF excitation with specified properties is given in [6]. Namely, a number of works, which reflect the results of studies where a uniform distribution of EMF on the surface of an immobile testing object (TO) is achieved by linear or nonlinear synthesis, is considered. Also in [6], ECP designs, in which a uniform excitation field is created by rectangular tangential and normal coils and due to the rotational excitation field, are analyzed.

As a result of the review, it was found that research on the creation of mobile ECPs, which provide uniform sensitivity in the testing zone, were not carried out according to the information available to the authors.

2. Background and the means for solving the problem

Linear and nonlinear synthesis of mobile circular SECP with a planar structure of the excitation system (ES) are described in a number of works by the authors [7-9]. In this case, options for the uniform and uneven placement of the coil sections along the radius, that located at the same height *z0* above the TO, are considered. The response surface is described by the dependence of the eddy currents density (ECD) distribution on several parameters $J = f(x, y, r)$, namely, the spatial coordinates x, y of the testing zone on the TO surface and the radius r of the excitation coil sections. The sought parameters for the linear synthesis procedure are the MMF *Iw* of each coil, and for the nonlinear one they are the coil radii and MMF. For such structure of ES the value of the reduced error of the homogeneity of the ECD in the testing zone is obtained from 9 to 12%, which is a satisfactory result.

The authors have also carried out a number of studies of circular SECP [10]. The probes had a volumetric homogeneous ES structure both with a uniform arrangement of sections Δr = const, Δz = const, and with an uneven one – Δr = var, Δz = var, where Δ is a parameter increment. To solve such a synthesis problem, a multiparametric ECP metamodel $J = (x, y, r, z0)$ was previously created, the construction features of which are considered in [10]. The obtained results of numerical experiments demonstrate the advantages of the synthesized volumetric ES structures in comparison with planar ones to ensure the requirements of uniformity.

At the same time, in addition to the considered ES structures with circular turns, there are also ESs in the form of rectangular frames with different positions relative to the TO, for example, parallel to the TO or perpendicular to it. Therefore, it is advisable to investigate a frame probe with a planar ES structure, consisting of a set of normal coils (see Fig. 1).

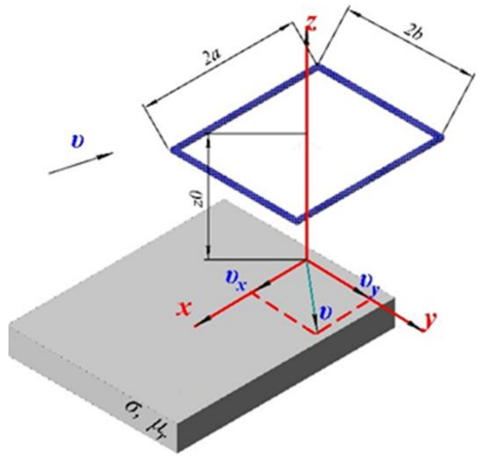

Fig. 1 *The source of the exciting field in the form of a rectangular turn.*

3. Solution of the problem

The purpose of the work is to create a method for linear surrogate synthesis of a frame non-coaxial ECP with a planar structure of the ES and uniform sensitivity in the testing zone. The method is provided by using a stochastic extremum search algorithm.

Before considering the SECP of a planar structure with a frame ES, let us first dwell on an EMF excitation source in the form of a single rectangular turn, which is a constituent element of such a structure. A rectangular turn with dimensions a x b is supplied with alternating current I and frequency ω and is located at a height *z0* above the TO of thickness d with constant specific electrical conductivity σ and magnetic permeability μ_r (see Fig. 1). The medium is considered linear, isotropic and homogeneous one. The velocity of the coil movement $\vec{\upsilon} = (\upsilon_x, \upsilon_y, 0)$ relative to the TO is constant.

The interaction of the field source in the form of a single turn with the TO is determined by the ratios of the complex components of the magnetic induction along the spatial coordinates B_x, B_y, B_z. They are obtained as a result of solving Maxwell's differential equations [11, 12] under the condition of continuity of tangential $H_{1t} = H_{2t}$ and normal $B_{1n} = B_{2n}$ components of the field at the interface between media 1 (air) and 2 (TO medium):

$$B_x = -j\frac{\mu_0 \cdot \mu_r \cdot I}{2\cdot\pi^2}\cdot\int\limits_{-\infty}^{\infty}\int\limits_{-\infty}^{\infty}\frac{\sin(a\cdot\xi)\cdot\sin(b\cdot\eta)}{\eta\cdot\left(1-e^{2\cdot\gamma\cdot d}\right)}\times$$
$$\times\left[\left\{-(1+\lambda_0)\cdot e^{2\cdot\gamma\cdot d}+\nu_0\cdot e^{\left(\gamma-\sqrt{\xi^2+\eta^2}\right)\cdot d}\right\}\cdot e^{\gamma\cdot z}+\right.$$
$$\left.+\left\{1+\lambda_0-\nu_0\cdot e^{\left(\gamma-\sqrt{\xi^2+\eta^2}\right)\cdot d}\right\}\cdot e^{-\gamma\cdot z}\right]\times$$
$$\times e^{-z0\cdot\sqrt{\xi^2+\eta^2}}\cdot e^{-j(x\cdot\xi+y\cdot\eta)}d\xi d\eta \qquad (1)$$

$$B_y = -j\frac{\mu_0 \cdot \mu_r \cdot I}{2\cdot\pi^2}\cdot\int\limits_{-\infty}^{\infty}\int\limits_{-\infty}^{\infty}\frac{\sin(a\cdot\xi)\cdot\sin(b\cdot\eta)}{\xi\cdot\left(1-e^{2\cdot\gamma\cdot d}\right)}\times$$
$$\times\left[\left\{-(1+\lambda_0)\cdot e^{2\cdot\gamma\cdot d}+\nu_0\cdot e^{\left(\gamma-\sqrt{\xi^2+\eta^2}\right)\cdot d}\right\}\cdot e^{\gamma\cdot z}+\right.$$
$$\left.+\left\{1+\lambda_0-\nu_0\cdot e^{\left(\gamma-\sqrt{\xi^2+\eta^2}\right)\cdot d}\right\}\cdot e^{-\gamma\cdot z}\right]\times$$
$$\times e^{-z0\cdot\sqrt{\xi^2+\eta^2}}\cdot e^{-j(x\cdot\xi+y\cdot\eta)}d\xi d\eta \qquad (2)$$

$$B_z = \frac{\mu_0 \cdot \mu_r \cdot I}{2\cdot\pi^2}\cdot\int\limits_{-\infty}^{\infty}\int\limits_{-\infty}^{\infty}\frac{\left(\xi^2+\eta^2\right)\cdot\sin(a\cdot\xi)\cdot\sin(b\cdot\eta)}{\xi\cdot\eta\cdot\gamma\cdot\left(1-e^{2\cdot\gamma\cdot d}\right)}\times \qquad (3)$$
$$\times\left[\left\{-(1+\lambda_0)\cdot e^{2\cdot\gamma\cdot d}+\nu_0\cdot e^{\left(\gamma-\sqrt{\xi^2+\eta^2}\right)\cdot d}\right\}\cdot e^{\gamma\cdot z}-\right.$$
$$\left.-\left\{1+\lambda_0-\nu_0\cdot e^{\left(\gamma-\sqrt{\xi^2+\eta^2}\right)\cdot d}\right\}\cdot e^{-\gamma\cdot z}\right]\times$$
$$\times e^{-z0\cdot\sqrt{\xi^2+\eta^2}}\cdot e^{-j(x\cdot\xi+y\cdot\eta)}d\xi d\eta$$

where $\gamma = \sqrt{\begin{array}{l}\xi^2+\eta^2 - j\times\sigma\times\mu_0\times\mu_r\times\left(\upsilon_x\times\xi+\upsilon_y\times\eta\right)+\\ +j\times\omega\times\sigma\times\mu_0\times\mu_r\end{array}}$;

$$\lambda_0 = \frac{\left\{\gamma^2-\mu_r^2\cdot\left(\xi^2+\eta^2\right)\right\}\cdot\left(1-e^{-2\cdot\gamma\cdot d}\right)}{\left(\gamma+\mu_r\cdot\sqrt{\xi^2+\eta^2}\right)^2-\left(\gamma-\mu_r\cdot\sqrt{\xi^2+\eta^2}\right)^2\cdot e^{-2\cdot\gamma\cdot d}};$$

$$\nu_0 = \frac{4\times\mu_r\times\gamma\times\sqrt{\xi^2+\eta^2}\times e^{\left(\sqrt{\xi^2+\eta^2}-\gamma\right)\times d}}{\left(\gamma+\mu_r\times\sqrt{\xi^2+\eta^2}\right)^2-\left(\gamma-\mu_r\times\sqrt{\xi^2+\eta^2}\right)^2\times e^{-2\times\gamma\times d}};$$

$\mu_0 = 4\cdot\pi\cdot10^{-7}$ H/m – the magnetic constant in vacuum; $j = \sqrt{-1}$;

ξ, η – variables of integration.

The mathematical model of the ECD distribution on the TO surface is determined through the partial derivatives of the magnetic induction components (1) - (3) with respect to spatial coordinates. Fig. 2 shows the ECD distribution obtained using a mathematical model for a single frame turn of 15 x 15 mm. The ECD distribution has a substantially non-linear characteristic in the testing area. It is possible to improve the distribution, namely to bring it closer to the desired uniform one (see Fig. 2), using a system of coils of various ES structures, as it is shown by the authors using the example of circular ECPs [7-10].

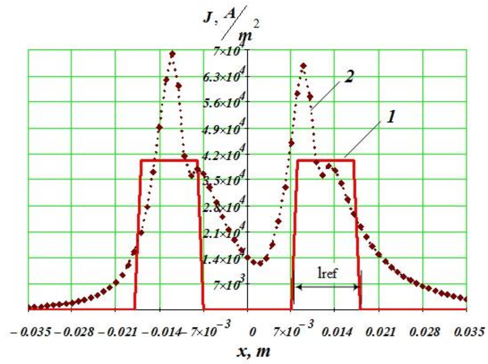

Fig. 2 *ECD distribution on the TO surface: 1 - desirable; 2 - created by a single turn of rectangular shape.*

The planar structure of the ES of a rectangular shape is a set of sectional coils connected in series with the dimensions of the sides a_i x b_i and a rectangular section, the width and height of which for each coil is individual q_i x τ_i (see Fig. 3). The coils are switched on oppositely or matched "across the field" and are located at the same average height $z0_m$ above the TO. In this case, each i-th from M excitation coils ($i = 1, ..., M$) is located in space uniformly Δa = const, Δb = const (see Fig. 3).

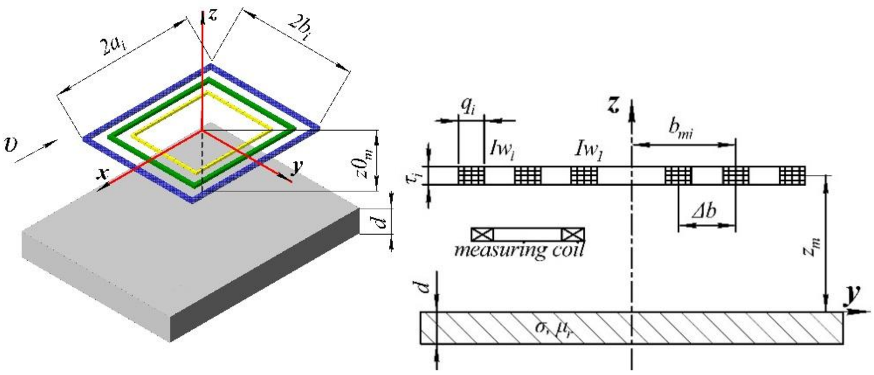

Fig. 3 *Planar structure of ES of rectangular shape.*

The synthesis problem of a rectangular coils system is formulated in an optimization formulation by minimizing a quadratic functional [7]. The analytical mathematical model for calculating the ECD distribution, which is created by a real system of coils, taking into account their transverse section, is cumbersome and complex. Since, in addition to improper multiple integrals of the first kind, the model also contains additional integration over the cross-sectional area of the coil. Therefore, the technology of surrogate optimization is used to implement the problem of optimal synthesis in order to reduce the resource consumption of computations. The main stages of the technology are described in [7, 8, 13].

According to the surrogate optimization algorithm, the first stage is the construction of an ECP metamodel based on a computer experiment design. Since the topology of the response hypersurface is complex, the computer experiment design for the multidimensional plan is based on a combination of Sobol's LP_τ-sequences. These sequences have the best indicators of centered and cyclic divergence, namely sequences $\left(\xi_6, \xi_7, \xi_{12}\right)$ [14].

Among a wide class of methods for constructing metamodels [15], taking into account their advantages and disadvantages for the approximation of multidimensional response surfaces, a heuristic method based on artificial neural networks (NN) was chosen, namely RBF - neural networks with a nuclear Gaussian activation function. At the same time, as has been repeatedly demonstrated in a number of works [7-9], it is inappropriate to use a single RBF-neural network given the large error of the metamodel obtained in this way. Therefore, the study uses a hybrid approach with the simultaneous use of search area decomposition and associative techniques of NN [7, 15]. Thus, metamodels for each subdomain using additive NN regression were obtained [15, 16]. At the same time, to improve the accuracy, a bagging-procedure for forming subsamples was used. For the formation of the NN committee, the best networks were selected according to the indicators of the coefficient of determination R^2, the ratio of standard deviations *S.D.ratio*, mean absolute percentage error *MAPE,%*. Then the output of each NN stage is formed by averaging over an ensemble of NNs with a performance of more than 90% [7, 9, 15].

In what follows, we restrict ourselves to considering the particular case of a rectangular frame, namely a square frame, when the average dimensions are equal to $a_{mi} = b_{mi}$ and, respectively, the increment Δ of the parameter is constant $\Delta a = \Delta b = \text{const}$. The metamodel, as a function of three parameters $\hat{J}=f(x, y, a_m)$, is constructed for the movable structure of the ES in the form of a complex of square-shaped ampere-turns. To construct a metamodel, the ranges of variation of the variables are as follows: spatial coordinates of the testing zone $x = -35 ... 35$ mm; $y = 0 ... 25$ mm; dimensions of ES coils $a_m = 3 – 15$ mm. In this case, according to the size of the coil am, the search area is divided into six subregions I_a ($3 \le a < 5$ mm), II_a ($5 \le a < 7$ mm), III_a ($7 \le a < 9$ mm), IV_a ($9 \le a < 11$ mm), V_a ($11 \le a < 13$ mm), VI_a ($13 \le a \le 15$ mm). All other parameters are constant and amounted to: $d = 10$ mm, $z_m = 3$ mm, $\upsilon = (40,0,0)$ m/s, frequency of the excitation current $f = 1$ kHz, electrophysical parameters of the TO material, respectively, $\sigma = 3.745 \cdot 10^7$ S/m and $\mu_r = 1$.

As a result, metamodels, for which the value of *MAPE,%* for different subranges is from 7.38 % to 14.91 % when teaching NN and, respectively, from 7.97 % to 14.24 % when reproducing the response surface using NN, were obtained. The reproduction of the response surface was performed on the number of reproduction points $N_{reproduction}$ that is larger than number of training points $N_{training}$ using a formula describing the output of an RBF-neural network [10].

Next, the problem of linear optimal synthesis was solved. In the objective function formula, the obtained RBF-metamodel of ECP was used instead of the "exact" mathematical model.

At the same time, the desired ECD distribution, which must be obtained as a result of solving the problem, was set, namely, the U-shaped distribution of ECD with intensity $J_{reference} = 40000$ A/m^2 in the testing zone ($7 \le x \le 17$) mm (see Fig. 2 graph 2).

To solve nonlinear inverse problems, it is advisable to apply stochastic algorithms for finding the global extremum [17]. In this research, the solution using several algorithms is obtained. First of them is a hybrid algorithm based on the genetic one with local search using the Nelder-Mead simplex method. The second is a swarm of PSO-RND particles with a random link topology strategy. In addition, the next one is a population metaheuristic optimization algorithm by a swarm of particles with evolutionary formation of the swarm composition. It is a low-level hybridization of the genetic algorithm and the PSO algorithm. As a result of the solution of the nonlinear inverse problem, the MMF Iwi of each ES coil was determined, which together provide an approximation of the created ECD distribution to the specified on the TO surface in the testing zone.

4. Results and discussion

For numerical simulation, the variants of ES structures with a different number of square coils $M = 3 - 5$ were specified, the distance between which is uniform $\Delta a = \text{const}$ (see Fig. 3). A preliminary analysis of the synthesis results allows one to select several ES structures. They have the best approximations to a uniform U-shaped ECD distribution, the width of which in the testing zone is $l_{ref} = 10$ mm. The numerical results of solving the synthesis problem are presented in Table 3.

Table 3: *Results of linear synthesis of the ES frame probe with different structures*

№	*Synthesized excitation systems*					
	M=3		*M=4*			
			variant 1		*variant 2*	
	a, mm	*Iw*, A×turns	*a*, mm	*Iw*, A×turns	*a*, mm	*Iw*, A×turns
1	6.5	-0.656	4.5	-0.421	6.5	-0.898
2	10.5	1.5	7.5	0	9.16	1.24
3	14.5	0.75	10.5	1.01	11.82	0.503
4			14.5	0.364	14.48	0.343

In table 3 the sign "-" for MMF means the opposite connection of the coil.

For synthesized ESs, according to "exact" mathematical expressions (1) - (3), the results of the ECD distribution along the Ox axis were obtained, as shown in Fig. 4, 5 (graph 1). In these figures, graph 2 is a given desired ECD distribution in the testing zone. Also, for comparison, these graphs show the ECD distribution created by a single rectangular turn (graph 3).

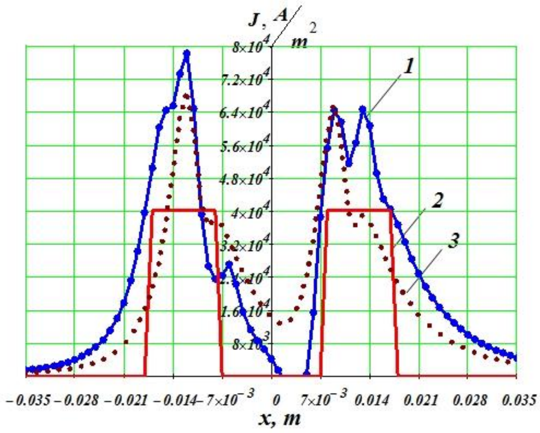

Fig. 4 *ECD distribution created by the ES structure of three coils.*

For clarity, the results of numerical experiments obtained as a result of linear synthesis of SECP are shown in Fig. 6 by the lines of the ECD level.

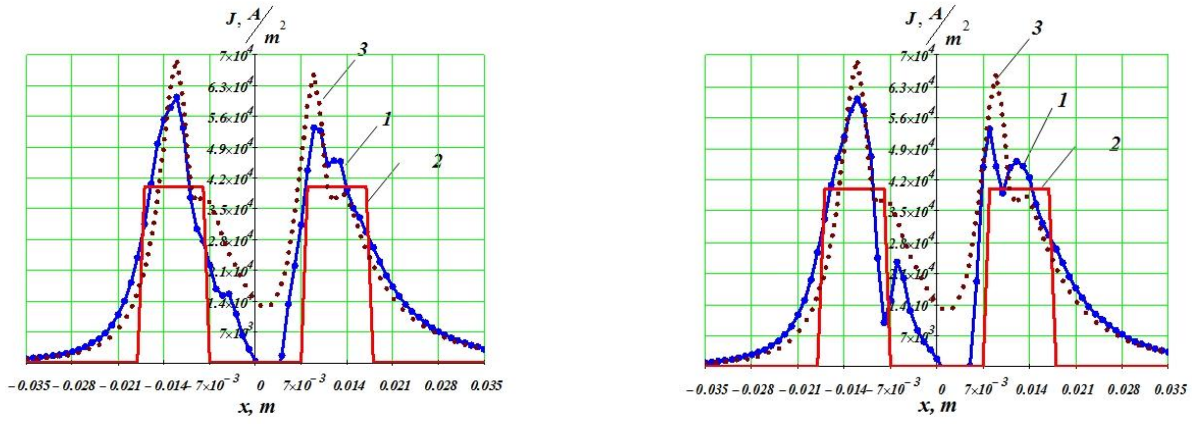

a) b)

Fig. 5 *ECD distribution, created by the ES structure of four coils: a) option 1; b) option 2.*

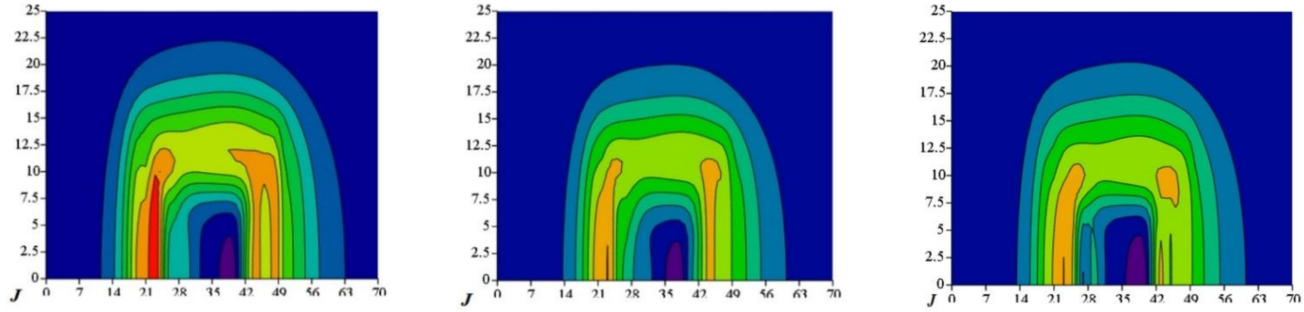

a) b) c)

Fig. 6 *ECD distribution in the form of level lines, obtained as a result of linear synthesis of ES structures: a) for three coils; b) for four coils, option 1; c) for four coils, option 2.*

Comparative visual analysis of the width of the uniform ECD distribution of the obtained ES structures with a different number of coils shows almost the same result. However, the preference must be given to a structure that provides it with their smaller number, that is, $M = 3$.

If the synthesized ES structure is compared with a single rectangular turn in the sense of the uniform ECD distribution created by them, then, undoubtedly, the best results were obtained for the planar ES, which is illustrated by the graphs in Figs. 4, 5

Thus, in the research by numerical experiments, the efficiency of solving the problem of linear synthesis of a frame ECP with a planar structure of the ES is shown.

Analysis of the results of linear synthesis indicated that it makes sense to carry out additional studies using nonlinear synthesis in order to clarify the geometric dimensions of the sectional coils.

5. References

[1] Rosado L.S., Gonzalez J.C., Santos T.G., Ramos P.M., Piedade M. Geometric optimization of a differential planar eddy currents probe for non-destructive testing. Sensors and Actuators A: Physical. - 2013. - V. 197. - P. 96-105. https://doi.org/10.1016/j.sna.2013.04.010

[2] Su Z., Efremov A., Safdarnejad M., Tamburrino A., Udpa L., Udpa S. Optimization of coil design for near uniform interrogating field generation / Z. AIP Conference Proceedings. - 2015. - V. 1650. - P. 405–413. https://doi.org/10.1063/1.4914636

[3] Su Z., Ye C., Tamburrino A., Udpa L., Udpa S. Optimization of coil design for eddy current testing of multi-layer structures. International Journal of Applied Electromagnetics and Mechanics. - 2016. – V. 52. - № 1-2. - P. 315-322. https://doi.org/10.3233/JAE-162030

[4] Repelianto A.S., Kasai N., Sekino K., Matsunaga M. A Uniform Eddy Current Probe with a Double-Excitation Coil for Flaw Detection on Aluminium Plates. Metals. - 2019. - № 9. - Article № 1116. https://doi.org/10.3390/met9101116

[5] Liu Z., Yao J., He C., Li Z., Liu X., Wu B. Development of a bidirectional-excitation eddy-current sensor with magnetic shielding: Detection of subsurface defects in stainless steel. IEEE Sensors J. - 2018. - V. 18. - № 15. - P. 6203-6216. https://doi.org/10.1109/JSEN.2018.2844957

[6] Halchenko V.Ya., Trembovetskaya R.V., Tychkov V.V. Surface eddy current probes: excitation systems of the optimal electromagnetic field (review). Devices and Methods of Measurements. 2020. № 1 (11). P. 42-52. https://doi.org/10.21122/2220-9506-2020-11-2-91-104

[7] Halchenko V.Ya., Trembovetska R.V., Tychkov V.V., Storchak A.V. Nonlinear surrogate synthesis of the surface circular eddy current probes. Przegląd elektrotechniczny. – 2019. - № 9. – P. 76-82. https://doi.org/10.15199/48.2019.09.15

[8] Trembovetska R.V., Halchenko V.Ya., Tychkov V.V. Optimal surrogate parametric synthesis of surface circular non-axial eddy current probes with uniform sensitivity in the testing zone / // Bulletin of the Kherson National Technical University. - 2019. – № 2(69). - Part 2. - P. 118-125. https://mkmm.org.ua/upload/%D0%92%D1%96%D1%81%D0%BD%D0%B8%D0%BA%20%D0%A5%D0%9D%D0%A2%D0%A3%20%D1%87%D0%B0%D1%81%D1%82%D0%B8%D0%BD%D0%B0%202.pdf

[9] Halchenko V.Ya., Trembovetska R.V., Tychkov V.V. Linear synthesis of non-axial surface eddy current probes. International Journal “NDT Days”. - 2019. - Vol. 2. - Issue. 3. - P. 259-268. https://www.ndt.net/article/NDTDays2019/papers/JNDTD-v2-n3-a03.pdf

[10] Trembovetska R.V., Halchenko V.Y., Tychkov V.V. Multiparameter hybrid neural network metamodel of eddy

current probes with volumetric structure of excitation system. International Scientific Journal «Mathematical Modeling». 2019. № 4 (3) P. 113-116.
https://stumejournals.com/journals/mm/2019/4/113

[11] Itaya T., Ishida K., Kubota Y., Tanaka A., Takehira N. Visualization of Eddy Current Distributions for Arbitrarily Shaped Coils Parallel to a Moving Conductor Slab. Progress in Electromagnetics Research M. 2016. Vol. 47. Pp. 1-12.
https://doi.org/10.2528/PIERM16011204

[12] Trembovetska R.V., Halchenko V.Ya., Tychkov V.V. Studying the computational resource demands of mathematical models for moving surface eddy current probes for synthesis problems. Eastern-European Journal of Enterprise Technologies. – 2018. - № 5/5 (95). - P. 39-46.
https://doi.org/10.15587/1729-4061.2018.143309

[13] Halchenko V.Ya., Trembovetskaya R.V., Tychkov V.V. Development of excitation structure RBF-metamodels of moving concentric eddy current probe. Electrical Engineering & Electromechanics. - 2019. - No 1. - P. 28-38.
https://doi.org/10.20998/2074-272X.2019.2.05

[14] Halchenko V.Ya., Trembovetska R.V., Tychkov V.V., Storchak A.V. The Construction of Effective Multidimensional Computer Designs of Experiments Based on a Quasi-random Additive Recursive Rd–sequence. Applied Computer Systems. 2020. Vol. 25, No. 1. Pp. 70-76.
https://doi.org/10.2478/acss-2020-0009

[15] Halchenko V.Ya., Trembovetska R.V., Tychkov V.V., Storchak A.V. Methods for creating metamodels: state of the question. Bulletin of Vinnitsa Polytechnic Institute. - 2020. - No. 4 (151). - P. 74 - 88.
https://doi.org/10.31649/1997-9266-2020-151-4-74-88

[16] Géron A. Hands-On Machine Learning with Scikit-Learn, Keras and TensorFlow: Concepts, Tools, and Techniques to Build Intelligent Systems. 2nd Edition. O'Reilly Media, Inc. 2019. 856 p.
ISBN-10: 1492032646.

[17] Halchenko V.Ya., Yakimov A.N. Population Metaheuristic Optimization Algorithms by a Particles Swarm: A Study Guide. Cherkasy. Publ. by Tretyakov A.N., 2015.160 p.
ISBN 978-617-7318-06-3.

Modelling of wire extrusion process

Deyan Gradinarov[1], Nuray Hasan[1]
Institute of Metal Science, equipment, and technologies with Center for Hydro- and Aerodynamics “Acad. A. Balevski” at the Bulgarian Academy of Sciences[1]
gradinarov@ims.bs.bg, hasan@ims.bas.bg

Abstract: *It is created computer model of wire extrusion process with Matlab. The model is verified by comparing the simulated results with experimental.*
Keywords*: WIRE EXTRUSION PROCESS, EXTRUSION MODELLING, ALUMINIUM EXTRUSION*

1. Description of wire extrusion process and definition of the model

The extrusion process is an essential method for the production of wires and rods (shown in Fig.1). Metal shavings, powder or granules are usually placed in a closed cylindrical container – matrix. Pressure from a tight-fitting rotation piston is applied. The piston rotates at a certain angular velocity. Due to the friction between the piston and the metal in the cylindrical container, heat is generated. Due to the heating and the applied pressure, plastic deformation occures in the metal raw material. The metal begins to come out through external channel in the piston, cools and crystallizes in the form of a wire or rod.

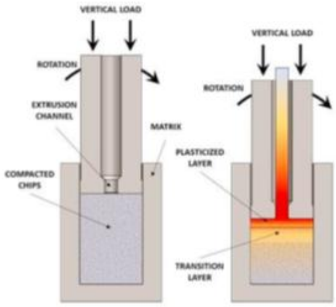

Fig. 1 *Principal structure of the wire extrusion process[1].*

The amount of generated heat in the extrusion process is determined according to:

$$Q = A = \vec{S_{sum}} x \vec{F_{fr}} = S_{sum} * cos\alpha * F_{fr} = S_{sum} * F_{fr} \qquad (1)$$

Where S_{sum} is total contact area;

F_{fr} – friction force;

$\alpha=90^o$ – angle between the piston surface and the metal in the cylindrical container

The total contact area is determined according to:

$$S_{sum} = n * S = \pi * r^2 * \omega * t \qquad (2)$$

Where $S=\pi r^2$ is the area of the piston;

r – radius of the piston;

$n=\omega*t$ – number of cycles the piston does;

ω – angular speed of the piston;

t – time of the extrusion process.

The friction force is determined according to:

$$F_{fr} = \mu * N \qquad (3)$$

Where N is the force applied by the piston;

μ – friction coefficient between the piston and the extruded metal.

By (1), (2) and (3) follows that the total amount of generated heat during the extrusion process is:

$$Q = \pi * \mu * \omega * N * r^2 * t \qquad (4)$$

To create the geometry of the model, the volume of the cylindrical container of the extruder is defined as the sum of elementary cubic cells along the X, Y and Z axes. These cells represent elementary volumes in each of which the given mathematical operations are performed.

The dimension of the created three-dimensional data array H (x, y, z) determines the size of the elementary volume for which the calculations are made and to which the value of the respective cell of this array is assigned. The size of this unit cell is determined according to:

$$d = \frac{D}{X} \qquad (5)$$

Where d is the size of the elemental cell;

D – the size of the element by the respective axis;

X – the dimension of the three-dimensional array along the respective axis.

The sampling time is determined by the number of steps. They are determined according to:

$$\Delta t = \frac{t_{extrusion}}{N_{steps}} \qquad (6)$$

Where Δt is the time of one sampling step;

$t_{extrusion}$ – the total amount of time of the extrusion process;

N_{steps} – the number of sampling steps.

Considering the generated heat energy for a single cell with extremely small dimensions and we have in mind (4) and (6), we have:

$$\Delta Q = \pi * \mu * \omega * N * r^2 * \Delta t = \pi * \mu * \omega * N * r^2 * \frac{t_{extrusion}}{N_{steps}} \qquad (7)$$

The increase in temperature depends on the amount of energy absorbed in the volume of the substance and is determined according to:

$$Q = cm\Delta T = c\rho_v V(T - T_0) \qquad (8)$$

Where c is specific heat capacity of the material;

m – the mass of the heated detail;

V – the volume of the heated part;

ρ_v – density of the material.

For elementary cell (8) is determined represented as:

$$\Delta Q = c\rho_v \Delta V(T - T_0) = c\rho_v d^3(T - T_0) \qquad (9)$$

The intensity of thermal conductivity is proportional to the temperature change in the considered direction. It is determined by Fourier's law:

$$Q = -\lambda S_x \frac{dT}{dx} \qquad (10)$$

Where Q is the full heat flow;

S_x – area of the heat flow conduction;

λ – thermal conductivity coefficient.

dT/dx – determines the rate of change of temperature in X axis (the direction in which the heat transfer is considered).

For elementary cell (10) is determined represented as:

$$\Delta Q = -\lambda d^2 * \frac{dT}{dx} \qquad (11)$$

The coefficient of thermal conductivity is a material constant that depends on temperature and is determined by:

$$\lambda = \lambda_0(1 + \alpha T) \qquad (12)$$

Where λ_0 is the coefficient of thermal conductivity at 0oC;

α – experimentally determined constant depending on the type of material.

The heat balance for each cell of the model is defined as the sum of the incoming heat transfer and the generated heat by friction on the one hand and the outgoing heat transfer and the accumulated heat in the cell on the other.

$$Q_{\text{incoming heat transfer}} + Q_{\text{generated heat by friction}} =$$
$$= Q_{\text{outgoing heat transfer}} + Q_{\text{accumulated heat in the cell}} \qquad (13)$$

2. Verification of the model

To create the computer model [2], the Matlab software product is chosen, which has very good computational and visualization capabilities, with the help of which the programming of the simulation model is greatly facilitated.

The verification of the model is performed by measuring the temperature of the extruded wire at the point where it comes out from the external in the piston channel. The extrusion is performed [3,4] using a hydraulic press for discrete extrusion ПХДЕ4000/ 1000, and the temperature measurement is non-contact – using an IL-92 pyrometer. The information is read via a USB interface from a laptop and processed in real time.

The process of extrusion is conducted with aluminium shavings. The coefficient of friction between aluminium and metal is considered to be 0.47. The applied pressure is 1000kN and the angular speed is 1rpm. The diameter of the extruded wire is 5mm. The temperature at the start of the extrusion process is T0 = 17oC.

Fig. 2 graphically presents the simulated and measured temperature. The temperatures reached by the extrusion process (simulated and measured) are below the melting point of aluminium, as this is the temperature to which the pyrometer has access to measure – the point at which the extruded wire exits the external in the piston channel.

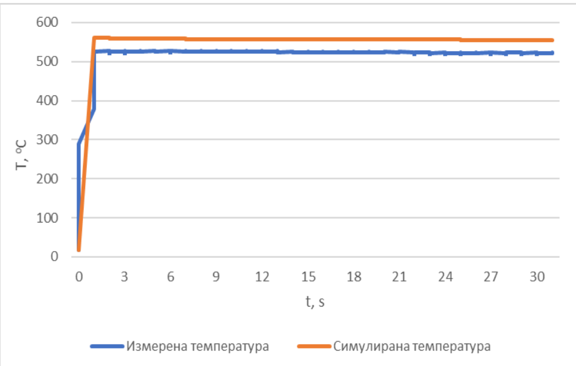

***Fig.2** Simulated and measured temperature reached in the extrusion process.*

Because of the nature of the process the piston moves inward into the cylindrical container, i.e. shifting the point at which the temperature is measured to a colder point of the wire. This displacement is not large and is relatively slow, as its effect is partially compensated by heating the piston, which leads to less heat loss in it.

The difference between the simulated and the measured temperatures is within 5-8%, as the simulated temperature is 30-35oC higher. The main reason is the simplification of the model and the complex definition of the influence of the piston.

3. Conclusions

It is created simulation model of the extrusion process from aluminium shavings. The model simulates temperature with 30-35oC higher than the measured.

The created model can be optimized by better defining of the influence of the piston of the extrusion press.

4. References

1. M. Samuel, 2003. A new technique for recycling aluminium scrap. Journal of Materials Processing Technology 135, 117–124
2. D. Gradinarov, Yu. Bijev, S. Todorov. „Simulation model of cross-wired EES process “. NDT days 2017, 2017, ISSN:1310-3940, 279-281
3. D. Gradinarov, N. Hasan, Y. Bijev, Оптимизация на Преса хидравлична за дискретна екструзия ПХДЕ4000/1000 чрез пирометър IL-92. International Journal "NDT Days", Bulgarian Society for NDT (BG S NDT), 2020, ISSN:2603-4646 (online)
4. N. Hasan, D. Gradinarov, Defining parameters for control of extruding wire by friction process. MATEC Web Conf. Volume 287, 2019 6th International BAPT Conference “Power Transmissions 2019”, 06003, 2019, DOI:https://doi.org/10.1051/matecconf/201928706003

Simulation of energy consumption for different types of hvac systems in a typical office building under tirana climate conditions

Albert Shira, Edmond Zeneli, Flamur Bidaj
Faculty of Mechanical Engineering – Polytechnic University of Tirana, Albania

ashira@fim.edu.al*

Abstract: *Thermal comfort and indoor air quality highly depend on proper design of Heating, Ventilation and Air Conditioned (HVAC) system. These system require large amounts of energy. Efficient use of energy leads to new concept design of HVAC systems. In this article, energy consumption in office building is analysed using Hourly Analysis Program (HAP) software. The aim of this research work is focused in estimation of office building energy consumption considering three different HVAC systems, respectively. Therefore, Variable Refrigerant Flow (VRF) system, HVAC 2-pipe and HVAC 4-pipe system were analysed with respect to energy consumption. A typical office building placed in Tirana, of 5000 m² of total area is used for this study.*

Keywords: HVAC 2-pipe, HVAC 4-pipe, VRF, ENERGY CONSUMPTION, OFFICE BUILDING,

1. Introduction

Heating Ventilation Air Condition (HVAC) systems purpose is to maintain good indoor air quality and provide thermal comfort. HVAC systems are among the largest energy consumers. The building sector accounts approximately 30% of total energy consumption in Europe and USA [1]. According to [2] in commercial buildings energy requirements of HVAC systems for heating account to 5%, thus 14% for cooling and 12% for ventilation of the area.

Optimal design and use of energy efficient systems challenges the everyday work of HVAC engineers. The selection of HVAC systems in a given building will depend on the climate, the age of the building, individual preferences of the owner, project budget and the architectural design of the building. Building sector has a significant increase in the recent years in Albania. The country has implemented EU and international standards for energy consumption. HVAC systems energy. In this study energy consumption in a selected office building has been analyzed using Hourly Analysis Program (HAP) software [3]. For this task three different HVAC systems are chosen, which refer to main systems applied currently in Albanian capital. Thermal calculations are based on mathematical models with respect to international standard ISO13790:2008 for energy use and thermal performance of buildings [4]. The goal of this work is to evaluate energy consumption in heating and cooling for the five floor office building with respect to HVAC system design.

2. Building characteristics

The office building used for this study is placed in the capital, Tirana. For energy simulations some critical information about building geometry, environment, equipment, and HVAC system is necessary. Energy prices in the Albanian market is a key factor for proper calculation and design of the system.

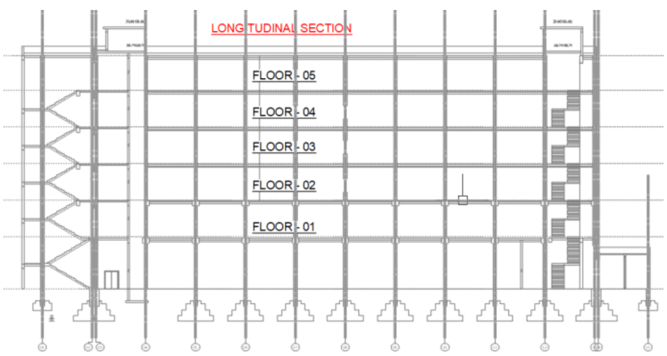

Fig.1. *Cross sectional view of the office building*

All the necessary information for the building has been collected for this study. In the table below are presented the data of the building. Area of each floor is 1000 m² and total area of the building is 5000 m².

Table 1: *Building characteristics and outdoor condition data*

Building characteristics	Value	Unit
Total Area	5000	m^2
Activity level	Office	
Ventilation requirements	2.5	L/s
Occupancy	105	people
Wall overall U coefficient	0.302	$W/m^{2o}C$
Roof overall U coefficient	0.304	$W/m^{2o}C$
U coefficient of Windows (Al with thermal break)	2.718	$W/m^{2o}C$
Summer design dry bulb temperature	35	^oC
Winter design dry bulb temperature	-2.2	^oC

The characteristics of the building elements are taken into account from the layout of the building and information about the use of the building is collected in place.

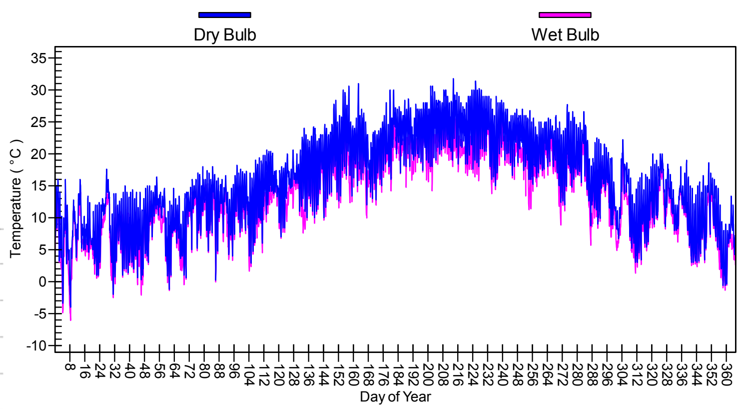

Fig.2. *Yearly temperature profile for Tirana*

The diagram of climate data for the capital Tirana is presented in Fig 2. The data collected for the period from January 1st to December 31 give the dry and wet bulb temperature profile for Tirana.

3. Results & Discussions

HVAC system on the office building considers three different technology solution. VRF systems have been developed since early 90s. These systems offer high energy efficiency with precise temperature and humidity control as well as high flexibility in modulating individual indoor units provide the desired cooling and/or heating in each area. VRF systems can save up to 40% energy over comparable unitary equipment.

HVAC two-pipe system are suitable when heating and cooling share hydronic piping. Each terminal unit Fan-Coil is equipped with one supply pipe and one return pipe. These systems are ideal for warm, tropical climate because heating load is rarely required.

HVAC four-pipe system are designed when heating and cooling require separate hydronic piping. Each Fan-Coil has two supply pipes and two return pipes. These system are suitable in multi-climate areas, because for example fan-coils can deliver simultaneous cooling and dehumidification by using cold and hot water at the same time. For this study energy consumption simulations are carried out. The HAP software was used for the building energy performance analysis. Each system performance is simulated separately. We have accepted building operation time and occupancy load do not change throughout the year.

The lighting is accepted at equal values for all office areas. The lighting equipment load is 5 W/m^2.

Electrical equipment load is 12 W/m^2.

According to [6] the activity level of the building premises is considered as office space with sensible heat 71.8 W/person and latent heat 60.1 W/person.

In Fig.3 and 4 is shown the distribution of heating and cooling building energy consumption during the year for the three systems taken into consideration.

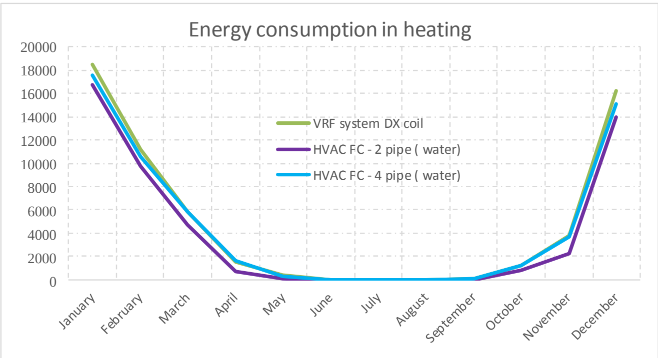

Fig.3. Building energy consumption in heating for three considered systems

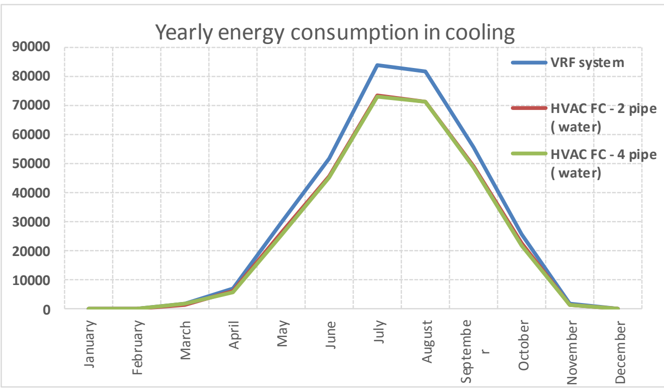

Fig. 4. Building energy consumption in cooling during the year in kWh/year

It is obvious that VRF systems use have a slightly increase on energy consumption during cooling and heating compared to other systems. For the cooling period the peak energy consumption results on 83,642 kWh, in July by the VRF system. Considering the building typology the cooling period starts in the early March and ends by in the beginning of November. For the remained period the cooling demand accounts to a few kWh, intended for server room in building.

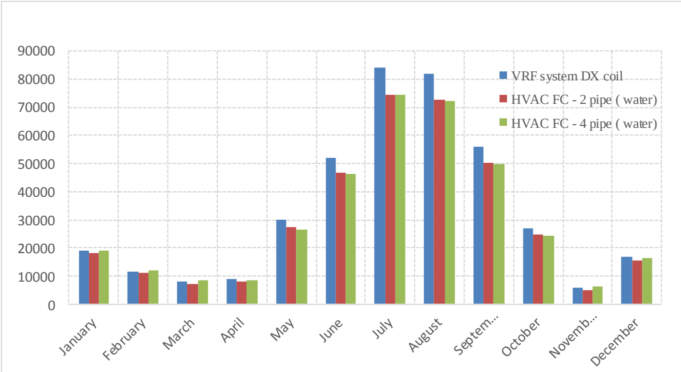

Fig.5. Building total energy consumption for each system in kWh/year

In Fig.5 a profile of total energy consumption of building is presented. As can be viewed from the graph energy consumption has an increase during midseason and peak in summer. This is due to building high cooling demand during summer. Therefore, total energy consumption in summer equals for VRF system equals to 84,134 kWh. For 2-pipe and 4-pipe HVAC systems this value is slightly lower compared to VRF. Another important indicator we can evaluate is specific energy consumption related to building total area. For this study calculated specific energy consumption of the building is shown in Fig.6.

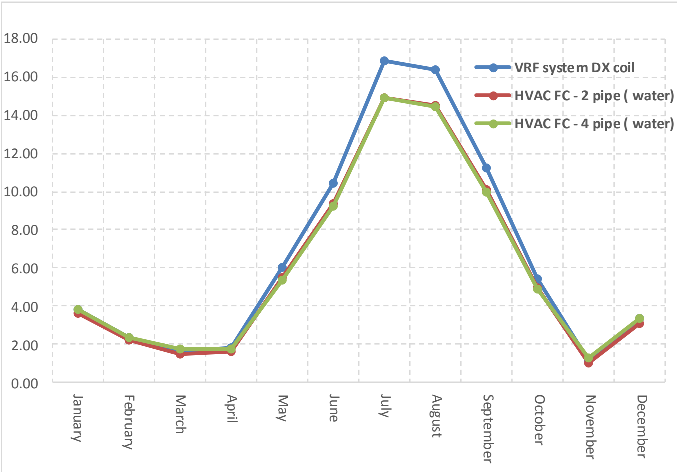

Fig.6. Specific energy consumption in kWh/m2 during the year

Specific energy consumption of office building for the entire period respecting indoor thermal comfort and air quality represent an important parameter for energy building performance. Energy calculation in HAP software shows that HVAC 2-pipes and 4-pipes system have a slightly decrease on energy consumption for same thermal conditions of the building. The difference in summer period when cooling demand increases is approximately 2 kWh/m^2. This is a considerable figure which should be taken into consideration when designing HVAC systems in office building for Tirana climate conditions.

4. Conclusion

In this article we shortly described the importance of HVAC systems related to energy requirements. Efficient use of energy calls for a new approach in HVAC system design considering the building character, architecture, environment, climate conditions energy prices, etc. A typical 5-floor office building placed in capital Tirana was used for this study. Three classic systems were analyzed in this work: VRF system, HVAC 2-pipes, HVAC 4-pipes system. All three systems are centralized HVAC and have great potential for energy savings. The physics of the building and yearly temperature profile of the city was taken into account. HAP software has given a profile of energy consumption for heating and cooling of the building during the year. Cumulative calculations shows the total energy consumption for each single system. As shown by simulations it is evident that for Tirana climate conditions the VRF system results on higher energy consumption compared to 2-pipes and 4-pipes HVAC system. Average specific energy consumption of three systems is 80.4, 72.3 and 73.1 kWh/m^2 respectively. No system cost considerations were taken into account for this study.

5. References

[1] EIA 2012-U.S Energy Information Administration. https://www.eia.gov/totalenergy/data/annual/pdf/aer.pdf

[2] L. Chretien, R. Becerra, N P Salts and E. A. Groll. System solution to improve energy efficiency of HVAC systems, *IOP Conference Series: Materials Science and Engineering*. Vol. 232, (2017), pp. 1-9.

[3] Carrier HAP Manual. https://www.ahi-carrier.gr/media/154466/e20s-HAP50_manual.pdf

[4] ISO 13790:2008. Energy performance of buildings-Calculation of energy use for space heating and cooling.

[5] ASHRAE design weather conditions. http://ashrae-meteo.info/

[6] Shira A., Dorri A., Bidaj F. *Energy consumption evaluation of the heating ventilation air condition through hourly analysis program software,* International Scientific Journal Industry 4.0, Issue 1/2020, ISSN 2534-8582 pp.27-28.

Multipurpose virtual model of a human body and its utilization in the traffic safety

Jan Špička[1,2], Jan Vychytil[1], Luděk Hynčík[1], Tomasz Bonkowski[1,2]

[1]New Technologies – Research Centre, University of West Bohemia in Pilsen, Univerzitní 8, Pilsen, 306 14, Czech Republic
[2]Faculty of Applied Sciences, University of West Bohemia in Pilsen, Univerzitní 8, Pilsen, 306 14, Czech Republic
E-mail: spicka@ntc.zcu.cz, jvychyti@ntc.zcu.cz, tomasz@ntis.zcu.cz, hyncik@ntc.zcu.cz

Abstract: *The aim of this work is the implementation of the virtual hybrid human body model Virthuman into the pedestrian traffic collision scenarios. The pedestrians are the most vulnerable traffic road users and they are exposed to a high risk and suffer with serious injuries and responsible for high number of death and injuries. The interest of the study of simulation of a car crash accident is motivated by the effort to decrease these numbers. The authors use a virtual model of the full human body called Virthuman here. This model was built based on combination of two modelling approaches, particularly multibody and finite element. Such method is call a hybrid approach and keeps advantages of both principles. The model was fully validated against published experimental data (particular body segment tests as well as full body tests) and was successfully used in the number of applications. The purpose of this paper is to present the model as a suitable tool for pedestrian collision modelling and injury risk assessment. Besides the description of the model, the examples of the application towards pedestrian safety are going to be presented here.*

KEYWORDS: *HUMAN BODY MODEL; VIRTHUMAN; PEDESTRIAN SAFETY; ACCIDENT RECONSTRUCTION; INJURY RISK*

1. Introduction

Pedestrians are the most vulnerable road users and they are exposed to a high risk in the collisions with the vehicles. The statistical data shows that pedestrians are still responsible for the second biggest number of fatalities and injuries on the road; about 2.000 in the Czech Republic [1, 2] 40.000 in the EU and 1.25 million around the globe annually, [1, 3, 4, 5].

Moreover, the recent studies in Europe indicate that the passenger cars are one of the most often involved in the collisions with the pedestrians. Figure 1 summarizes the distribution of the vehicle type participating in the pedestrian collisions in the Czech Republic in years 2009-2014 [6]

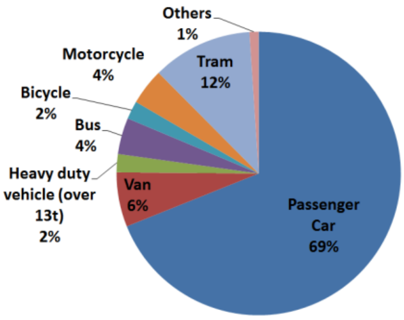

Figure 1: *Distribution of the vehicle type involved the pedestrian accident in the Czech Republic in 2009-2014*

Recently, the virtual human body models are being used more often and virtual approach in the biomechanical fields. The virtual prototyping in the automotive industry takes benefit from the numerical models of the humans. The models are mostly based on the finite element method, articulated rigid bodies (multibody) or a hybrid approach that combines advantages of both approaches. The review of the current state of biomechanical human body models is given for instance in [7, 8].

This work demonstrates the application of the virtual human body model Virthuman in various road traffic incidents including the pedestrian. Firstly, the Virthuman is described. Secondly, the model is used in the real accident reconstruction, sensitivity analysis of the gait posture during frontal car to pedestrian crash and simulation of such scenario, or development of new tram front-end design.

2. Methods

2.1. Virthuman

The Virthuman model is a hybrid model combining the two main modelling approaches, the deformable elements and rigid body segmentation within the multi-body (MBS) structure. The basic structure of the human is modelled using the multi-body and consists of rigid segments connected via kinematic joints. The anatomical shape of the human is modelled using finite element surface segments connected via non-linear springs and dampers to the basic MBS structure. Virthuman model can be easily used as a pedestrian, driver or passenger of a car. The Virthuman model is also a fully scalable human model taking the gender, age, size and weight of the particular subject into the account [9]. The scaling algorithm implemented in the model is based on a large anthropometric database [10] measured in the Czechoslovakia in 1980's. The example of a size variable Virthuman model is demonstrated in Figure 2, where a small child, a big male and an average female are shown.

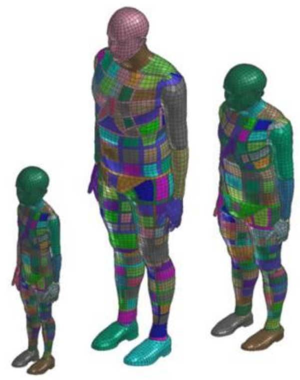

Figure 2: *Scaled Virthuman model. 6-year-old child, 110 cm, 17 kg (left); 40-year- old male, 190 cm*

The model was fully validated against a large set of validation tests and especially validated for the pedestrian impacts [11, 12]. The full-body tests as well as the detailed tests for the particular human body segments were performed to ensure the boofidelity of the Virthuman model. There is an automatic algorithm for evaluation of the specified criterion based on various mechanical quantities (e.g. contact force, acceleration, displacement, torques etc.), implemented in the model [13]. The list of the evaluated criterion is based on EuroNCAP rating and is available in [12], see Figure 3.

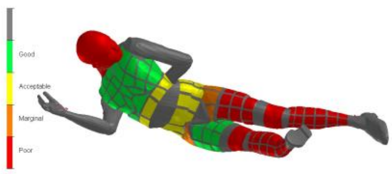

Figure 3: *Example of injury risk evaluation within Virthuman model*

3. Application example

The Virthuman model has a great benefit of the fast calculation time, a simple definition of any initial stature (position of the body), scaling algorithm (personalized subjects) and also the injury prediction. Thus, the model is very useful in the cases, where a large number of calculations is required or different postures and different occupants need to be analysed. It does not deal with the detailed injury of all tissues (hard or soft), since the model does not have any internal structures. However, it can still bring the knowledge of mechanical loading, which can be interpreted in the way of human injury. This paper presents several cases of Virthuman applications as a pedestrian.

3.1. Sensitivity analysis of the human gait posture on the injury

Sensitivity analysis of the frontal pedestrian-to-car collision is presented. The collision of the pedestrians with the vehicle can be divided into two phases: the primary contact (the human with the car) and the secondary contact (the human with the ground). Significant injuries can occur in both phases. The main focus of the research lays obviously on the primary contact [14, 15, 16, 17, 18, 19], since the ground contact depends on the material of the landing area, which is hardly to be improved. The research data from Yang [4] shows that a majority of the pedestrian accidents occurs while walking. In our previous work, [19], the authors were focused on the analysis of the human gait and its effect on the frontal crash with the vehicle [20]. The main effort was the analysis of the different gait postures and the walking speed of the pedestrian. The experimental measurement of the volunteer gait was used for identification of the particular body joints angles of rotation, see Figure 4.

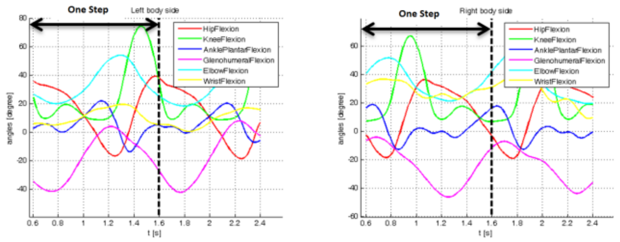

Figure 4: Angles of rotation in the human joints, Spicka et al. (2017)

The human gait was afterwards divided into 9 phases, see Figure 5.

Figure 5: *Human gait phases*

Consequently, the pedestrian was also rotated around the vertical axes, to capture the effect of the different directions of impact, see Figure 7. Authors used simple multibody structure of the external car-bonnet shape (m = 1200 kg, v_0 = 45 km/h) with the validated virtual springs and dampers [11, 21], to preserve the calculation time as shortest as possible, see Figure 6 and Figure 7.

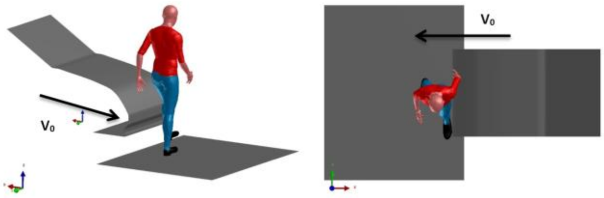

Figure 6: *Configuration of the testing collision*

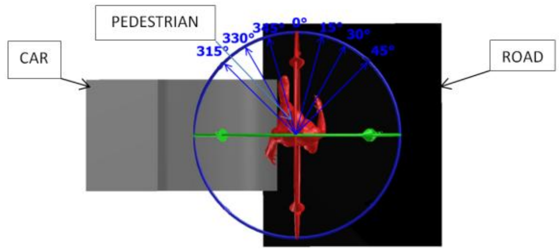

Figure 7: *Initial posture of the pedestrian with respect to the car*

Such analysis shows, how the initial posture of the pedestrian (especially position of the upper end lower extremities) can affect the overall kinematics and injury of the human.

3.2. Accident reconstruction

Next application example is a reconstruction of a real traffic collision between the car and the pedestrian. The specific pedestrian (defined by age, gender, size and mass) including her injury as well as the car (make and model, and the photo from the accident) were available. The accident protocol contains a description of the car damage and the injuries sustained by the pedestrian. The effort of the accident reconstruction was not only to meet the damage of the vehicle (shape and maximal bonnet intrusion), but also the pedestrian injury.

The goal was to find the initial position, that could result in such pedestrian injury and the car deformation and to test, if the available conditions could meet such results with the advantages of the numerical modelling. The defined accident involves the car Skoda Roomster 1.4 (the mass = 1205 kg, the dimensions 4.2 x 1.7 x 1.6 m and the initial velocity v_0 = 30 km/h) hitting the pedestrian (female, 77 years old, mass = 70 kg, the height = 167 cm) from her left side. The injury sustained by the pedestrian is summarised as follows, together with Abbreviated Injury Score (AIS) [22], see Figure 8:

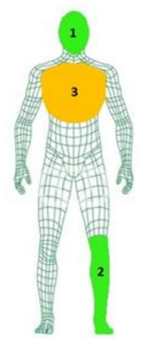

- Head contusion.
- Scapula fracture.
- Fracture of 3rd - 8th left ribs.
- Abruption of the L1 vertebra.
- Left ankle fracture.
- Left subtalar joint fracture.
- Left knee contusion and abrasion.
- **Total injury severity score ISS = 14.**

Figure 8: *Pedestrian injury*

amage of the car was only on the frontal part, mainly the right corner of the bonnet. The deformation of the frontal part of the car, i.e. the bonnet and the bumper, as well as overall configuration of the accident are highlighted in Figure 9.

Figure 9: *Deformed Skoda Roomster bonnet*

The goal was the reconstruction of the real collision with respect to the given initial conditions, which requires not only the pedestrian dynamics and injuries, but also the car damage to be as close to the real collision as possible. The exact position of the pedestrian was not known. However, with the advantages of the numerical model of the car, with the proper definition of the reinforcement and the materials, the authors met the injury of the female as well as the damage of the car in the certain level of accuracy.
The calculated head injury criterion (HIC) results in value equalling to 235, which corresponds to AIS 1 - 2 (which is in agreement with the accident protocol). The maximal calculated bonnet deformation was 4 - 5 cm.

3.3. Tram design safe for pedestrian

Virthuman model finds its advantages also in the railway vehicles passive research. The main point of this research is to reduce the severity of the consequences of a collision between a tram and a pedestrian. The work of Špirk [23] has tended to a new tram safety system as a proposal from the pedestrian, passenger and driver points of view, and connected with the preparation of a new tram regulation [24]. Such regulation defines the shape of the front end of the tram, as well as the collision scenario (initial velocity of 20 km/h) to be tested. The position of the pedestrian with respect to the tram is also specified. For assessment of the tram geometry, it is necessary to investigate in the various shape of tram face by the numerical simulations. The tram face can be divided into the finite number of linear planes with the finite number of shapes [23]. Each flat surface has its own stiffness, damping and slope (inclination angles: B_{ws} and B_y). Špirk in his work [25] used the definition of the segmented tram front face based on the regulation and brought a sensitivity analysis of the two main variables (the angles B_Y) on the HIC changes, see Figure 10 and **Грешка! Източникът на препратката не е намерен.**.

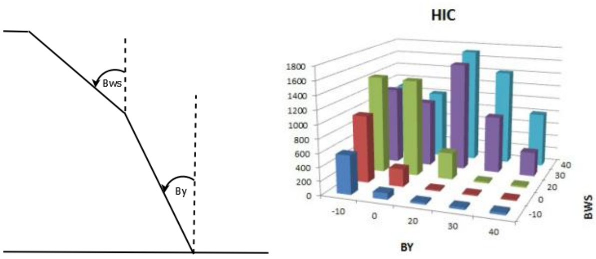

Figure 10: *Profile view of the tram the angles (left) and bar plot of the two main variables of the tram shape onto HIC value (right)*

During the tram design optimization, the authors were focused also on the influence of the lateral position of the pedestrian with respect to the tram, see Figure 11. The collision of the tram and pedestrian usually consists of scenario of pulling the pedestrian under the vehicle. Thus, the regulation defines the safety mechanism of the tram in the way, that the pedestrian cannot be pull under, moreover, it must be thrown latterly from the tram, not to be override after the landing.

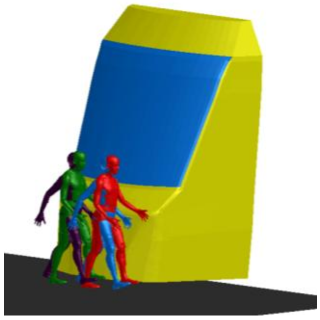

Figure 11: *Pedestrian initial positions with respect to the tram*

4. Discussion

The virtual human body model Virthuman presented in this paper shows its benefit in the road traffic field with the focused on the pedestrian. This work introduces the model in the several collision scenarios, occurring in the real world of traffic. It was shown, that the Virthuman model is a suitable and efficient tool in the modelling of the crashes between pedestrian and vehicle. The model was built based on hybrid approach, i.e. combination of finite element and multibody methods. Hence, it cannot provide detailed deformations and stress, of all the issues, as FEM can. However, with the advantage of injury prediction algorithm, it can result with the prediction of injury probability, which can be sufficient data in the numbers of applications. Moreover, with the benefit of the multibody structure, such model is easy to set-up in any initial position/posture of the human and thanks to the scaling algorithm, the variation of the population size, age and gender can be captured here.

5. Conclusion

This work introduced numerical model of the human called Virthuman as a useful tool for the pedestrian modelling. Such model takes advantages of the combine approach (MBS + FEM). Multibody method gives to the model benefit of scaling and positioning algorithm, while the deformable finite elements bring the local deformability to the model. The injury prediction algorithm is based EuroNCAP.

The previously described model Virthuman was used in the modelling of various road traffic scenarios consist of the pedestrian. Firstly, the model was used in the sensitivity analysis of the pedestrian gait on the collision (kinematics, dynamics and consequently the sustained injury). The second application of the Virthuman was the reconstruction of the real car to pedestrian accident, modelled based on the accident protocol only. The aim here was to use the provided data (pre-collision scenario, car make and model, the particular pedestrian, the car damage and the pedestrian injury) and numerically reconstruct the defined accident and to test, if the provided input data can meet the required output. The last example of the possible application of this model was the collision of the pedestrian with the tramway. The effort here is development of the tram front end, which could be safe for the human in case of accident.
However, the presented model is not limited only for the applications showed above. It can find the new purpose, not only in pedestrian and traffic industry. It has been successfully used also for small children modelling, which is generally taught task.

6. References

1. Besip, *Overview of the road accident in the EU* [online], *Besip*, Ministry of transportation, Available at: *http://www.ibesip.cz/cz/statistiky/statistiky-nehodovosti-v-evrope/prehled-vyvojedopravnich-nehod-v-eu*, (2016)
2. Policie ČR, *Overview of road accident in the Czech Republic in the 2014*, Directorate of Transport Police, Police Presidium

of the Czech Republic, Praha, Available at: http://www.policie.cz/clanek/statistika-nehodovosti-900835.aspx?Q=y2hudw09mw%3d%3d, (2015)
3. P. Ramamurthy, M.V. Blundell, C. Bastien, Y. Zhang, *Computer simulation of real-world vehicle pedestrian impacts*, International Journal of Crashworthiness, **Vol. 16(4**), pp: 351–363, (2011)
4. J. Yang, J. Yao, D. Otte, *Correlation of different impact conditions to the injury severity of pedestrians in real world accidents*, Proceedings of 19th International Technical Conf. Enhanced Safety of Vehicle, (2005)
5. WHO, World Health Organisation, *Global status report on road safety in 2015*, Available at *https://www.who.int/violence_injury_prevention/road_safety_status/2015/en/*, (2015)
6. TAČR TA04030689, *Development of active car bonnet with respect to the diversity of the human population and implementation of the biomechanical model of human body*. Intermediate report*,* (2015)
7. K. H. Yang, J. Hu, N. A. White, A. I. King, *Development of numerical models for injury Biomechanics research: A review of 50 years of publications in the Stapp Car Crash Conference*, No. 2006-22-0017. SAE Technical Paper, (2006)
8. S. Scataglini, P. Gunther, *DHM And Posturography*. Academic Press, (2019)
9. L. Hynčík, J. Špička, J., Maňas, J. Vychytil, *Stature Based Approach towards Vehicle Safety*, (No. 2015-26-0209), *SAE Technical Paper*, (2005)
10. P. Bláha, V. Šedivý, K. Čechovský, A. Kosová, *Anthropometric studies of the Czechoslovak Population from 6 to 55 years*, Czechoslovak spartakiade, **Vol. 1**, part 2, Praha, (1985)
11. J. Vychytil, J. Maňas H. Čechová, S. Špirk L. Hynčík, L. Kovář, *Scalable multi-purpose virtual Human model for future safety assessment*, (No. 2014-01-0534), SAE Technical Paper, (2014)
12. J. Vychytil, L. Hynčík, J. Maňas, P. Pavlata, R. Striegler, T., Moser, R. Valášek, R. *Prediction of Injury Risk in Pedestrian Accidents Using Virtual Human Model Virthuman: Real Case and Parametric Study*, (No. 2016-01-1511), *SAE Technical Paper*, (2016)
13. ESI, *Virthuman Postprocessing Manual, VPS Explicit MBS Model*, *Mecas ESI*, Rev, 2, (2015)
14. M. Hamacher, L. Eckstein, R. Paas, *Vehicle related influence of post-car impact pedestrian kinematics on secondary impact*, Proceedings of the International Research Council on the Biomechanics of Injury conference. **Vol. 40**. International Research Council on Biomechanics of Injury, (2012)
15. I. Han, R. M. Brach, *Throw model for frontal pedestrian collisions*, (No. 2001-01-0898), *SAE Technical Paper*, (2001)
16. C. K. Simms, D. P. Wood, *Effect of pre-impact pedestrian position and motion on kinematics and Injuries from vehicle and ground contact*, International Journal of Crashworthiness, Taylor & Francis, (2006)
17. Y, Suguru, T, Matsuhashi, Y. Matsuoka, *Simulation of car-pedestrian accident for evaluate car Structure*, Proceedings of the 26th Int. Tech. Conf. On the Enhanced Safety of Vehicles, Windsor (Canada), (1998)
18. D. P. Wood, C. K. Simms, D. G. Walsh, *Vehicle-pedestrian collisions: Validated models for Pedestrian impact and projection*, Proceedings of the Institution of Mechanical Engineers, Part D: Journal of Automobile Engineering, Vol 219(2), pp: 183-195, (2005)
19. J. Špička, J. Vychytil, J. Maňas, P. Pavlata, J. Motl *Modelling of Real Car-to-Pedestrian Accident: Comparison of Various Approaches in the Car Bonnet Modelling*, Proceedings of ECCOMAS Thematic Conference on Multibody Dynamics, Prague, (2017)
20. J. Špička, J. Vychytil, L. Hynčík, *Numerical analysis of a pedestrian to car collision: Effect of variations in walk*, Applied and Computational Mechanics, **Vol. 10(2),** (2017),
21. J. R. Kerrigan, D. B. Murphy, D. C. Drinkwater, C. Y. Kam, D. Bose, J. R. Crandall, J. R. *Kinematic corridors for PMHS tested in full-scale pedestrian impact tests*, In Experimental Safety Vehicles Conference, (2005)
22. K-U. Schmitt, P, Niederer, F. Walz, *Trauma biomechanics: Introduction to accidental injury*, Springer Science & Business Media, (2004)
23. S. Špirk, *The collision of unbelted passenger with assessment of various vehicle interior*, Proceedings of Manufacturing Technology, (2017)
24. STRMTG, *Technical Agency for ropeway and Guided Transport System*, The technical guides, Tramway front end design, Version 01, (2016)
25. S. Špirk, J. Špička, *Tramway front end design safe for pedestrian*, Proceedings of Applied and Computational Mechanics, (2018)

Motorcycle accidents reconstruction and simulation - application of hybrid human body model

Tomasz Bonkowski[1,*], Ludek Hyncik[1], Jan Spicka[1], Jan Vychytil[1]
Department of Biomechanical Human Body Models, New Technologies – Research Centre, University of West Bohemia, Univerzitní 8, 301 00 Pilsen, Czech Republic [1]
tomasz@ntc.zcu.cz

Abstract: *Motorcycle accidents with opposite vehicles are among the most difficult to reconstruct due to complicated kinematics and interactions between multiple participants. The Multi-Body System approach commonly applied in software packages as PC-Crash and Virtual-Crash, allows for proper reconstruction of the crash kinematics but did not take into account the full deformation of the vehicles and occupants. On the other hand, the Finite Element Method approach, especially the explicit formulation, used in the field of crashworthiness gives a way to describe the proper material behavior of the participant components during dynamic events. For the analysis of the accident, the full FEM approach becomes too complicated and time-consuming (both for preparation of the simulation and for the simulation run). The authors would like to propose a hybrid approach which couples and FEM and MBS models in VPS numerical environment (Pam-crash solver). This paper presents an analysis of the accident between the maxi-scooter and the opposite vehicle. As the representation of the PTW driver, a Virthuman hybrid human body model was used. This model in opposition to full FEM models allows the fast calculation of the simulation. Besides the kinematics of the accident, prescribed injury criteria were assessed on the human body model.*
Keywords*: VULNERABLE ROAD USERS, HUMAN BODY MODEL, VIRTHUMAN, MOTORCYCLE ACCIDENTS*

1. Introduction

An accident reconstruction is a procedure of creating the linkage between the causes and the effects of an accident. This procedure could be carried out in two ways. The first way is a backward-looking, in which the reconstruction starts from the known post- crash position of crash participants. The information about the deformation and the post-crash movement guide to the impact speed, and then to the driving speed. The second way of the accident reconstruction is a forward reconstruction.[1,2]

In the forward reconstruction, the accident is replicated by the numerical model. This method aims to replicate the final position by the solution of the model. Proper numerical models of participants and interaction between them are crucial to conducting the backward reconstruction procedure. For a regular PTW to a car accident, at least four numerical models are required (car, PTW, rider, helmet). Due to its multi-directional validation and scaling possibility, the Virthuman model can be used as a representation of the PTW rider. Moreover, the classical injury criteria like the HIC and the Nij could be assessed on the Virthuman model.

2. Materials

The cases were simulated in the numerical environment: Virtual Performance Solution (former PamCrash). The simulation was performed for the FEM models (the OV, the helmet) using an explicit approach. The main aim of the simulation was the reconstruction of the PTW occupant injury pattern. Due to the nature of the Virthuman [3] (MBS), the injuries could be only found by monitoring the nodal accelerations and forces which appear in the joints [4,5]. Based on these parameters, the injury criteria can be calculated (e.g. HIC - head injury criteria).

During the simulation, four macroscopic objects were used (the PTW, the OV, the occupant, and the helmet) [6]. Before starting the numerical calculation, these objects must be positioned and coupled. The procedure for coupling was as follows:

- ► Virthuman scaling according to the PTW occupant description
- ► Coupling Virthuman to the helmet
- ► Positioning Virthuman to a sitting position,
- ► Coupling Virthuman to the PTW (at the contact points),
- ► Positioning the PTW with the occupant (according to the backward reconstruction),
- ► Setting the initial velocities of the PTW and the OV.
- ► Injury criteria evaluation

After the simulation, two injury criteria were evaluated:

- ► Nij - normalized neck injury criterion,
- ► HIC - head injury criterion.

The Nij injury criterion could be calculated as follows [7]:

$$N_{ij} = \frac{F_Z}{F_{int}} + \frac{M_Y}{M_{int}},$$

where:
F_Z - the axial load,
F_{int} - the critical intercept value of load used for normalization,
M_Y - the flexion/extension bending moment,
M_{int} -the critical intercept value for moment used for normalization.

The HIC can be defined as follows [7]:

$$HIC = \left\{ \left[\frac{1}{t_2 - t_1} \int_{t_1}^{t_2} a(t)dt \right]^{2.5} (t_2 - t_1) \right\}_{max}$$

where:
t_1 - the initial time of the interval in which the HIC has a maximum value,
t_2 - the final time of the interval in which the HIC has a maximum value,
$a(t)$ - the magnitude of the acceleration of the head center of gravity.

2.1 Case 1

The first step for an accident simulation is the positioning of the vehicles and the occupant. In Case 1, the OV and the PTW were positioned according to the figures from the case description. The angle between the vehicles was equal to 114 deg.

- ► OV: Ford Fiesta (2004) with a mass of 1300 kg,
- ► The PTW mass: 260 kg (vehicle with driver)
- ► The PTW speed: 55 km/h,
- ► The OV speed: 10 km/h.

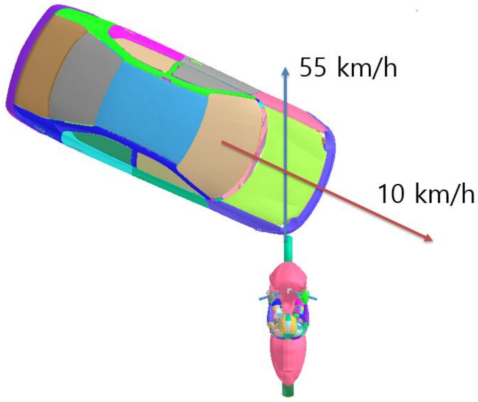

Figure 1. *Case 1 setup.*

2.2 Case 2

According to the procedure, the first step was Virthuman scaling. The basic model was scaled to the anthropometric parameters of the real PTW occupant. Next, the model was positioned, coupled with the helmet and coupled with the motorcycle. Then the OV model was trimmed to the mass reported in police records (1130 kg). After these steps, the PTW model was positioned against the OV model (Figure 2.). The angle between the vehicles was approximately 111 deg.

- OV: Fiat Grande Punto (2009) with a mass of 1130 kg,
- The PTW mass: 260 kg
  (vehicle with driver)
- The PTW: 56 km/h,
- The OV: 9.5 km/h.

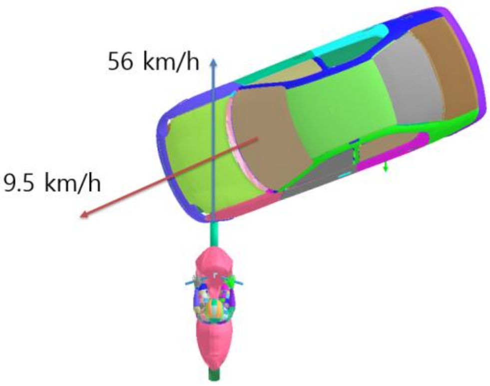

Figure 2. *Case 2 setup*

3. Results

3.1 Case 1

The kinematics of the accident is shown in the foregoing figures. All sub-phases of the PTW crash can be easily seen. Firstly, the front fork of the PB is compressed (0 – 30 ms). Next, the fork starts to deform (30 – 60 ms). The third step of the kinematics is the rotation of the PTW around the contact point.

During these sub-phases, the movement of the occupant can be described as follows. Firstly, the body of the driver starts to slide out from the seat, due to the PTW´s loss of speed. The occupant´s hands start to be compressed against the handlebar. After reaching the 450 N of the contact force between the hands and the handlebar, the contact ends. The upper part of the driver´s body starts to overtake the PTW. The lower part of the body is continuously compressed by the inertia forces on the PTW front frame. Due to this, the lower extremities are blocked by the PTW frame. This situation results in the appearance of the torque which acts on the rider´s body. This torque results in rotation of the occupant around the point of the abdomen – motorcycle contact (90 - 120 ms). Because of the body rotation, the occupant finally hits the OV hood with the head.

- 0 – 30 ms sliding on the seat
- 30 ms reaching maximum handlebar grip force (450 N)
- 30 – 60 ms continuous sliding from the seat
- 60 ms first contact between the occupant´s abdomen and the PTW frame
- 60 - 180 ms rotation of the body until the head-to- hood impact (175 - 185 ms).

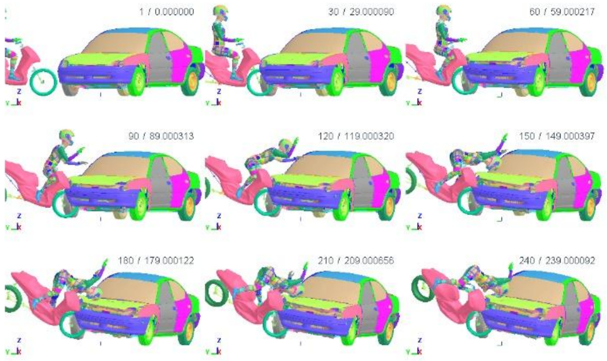

Figure 3. *Case 1 kinematics.*

The initial momentum and angle of the OV result in the change of the PTW path (the path starts to rotate clockwise). This situation results in contact between the left side of the PTW and the left leg of the occupant (150 - 240 ms). The contact force between the leg and the PTW side can result in an extensive leg injury. By analyzing the acceleration, which was acting on the head center of gravity (COG), the head injury criteria (HIC) can be calculated. In the reconstructed case the HIC is equal to 489 (Figure 4.). This value is in line with the medical examination of the PTW driver – the examination did not find injuries higher than AIS1.

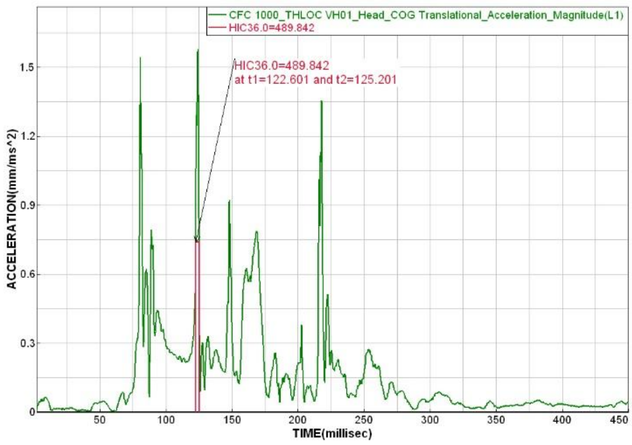

Figure 4. *Case 1 HIC assessment.*

After the filtration, the Nij was calculated. The calculation has been placed in the 50th percentile male corridor (Figure 5.). This figure shows that the corridor has been exceeded. This situation occurs because of the high peak of the neck extension force at 75 ms and 120 ms. However, the medical examination of the area did not report any neck injuries.

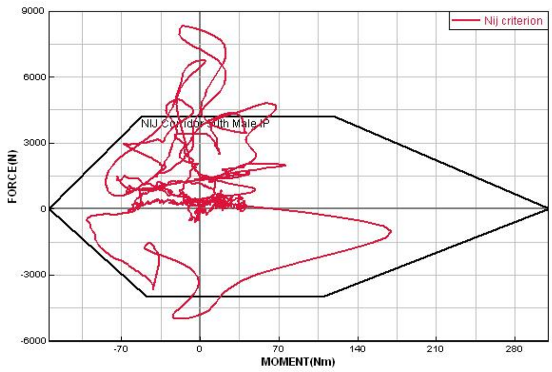

Figure 5. *Case 1 Nij corridor.*

3.2 Case 2

The kinematics of the crash are presented in the foregoing figures. The crash starts with the first contact between the PTW front wheel and the left fender of the OV. In the first 20 ms, the fork of the PTW is exposed to compression. After this period, the fork starts to bend (20 - 45 ms) until the first contact between the PTW front wheel and the PTW frame. At 45 ms, the PTW starts to rotate around the vehicles´ contact point (Y-axis of the PTW). This results in the rear part of the PTW lifting.

During the crash, the PTW driver´s movement passes through the following steps:

- 0 – 30 ms sliding on the seat
- 30 ms reaching maximum handlebar grip force (450 N) – releasing the hands
- 30 – 60 ms continuous sliding from the seat
- 60 ms first contact between the occupant´s abdomen and the PTW frame
- 60 - 180 ms rotation of the body until the head-to- hood impact (175 - 185 ms)

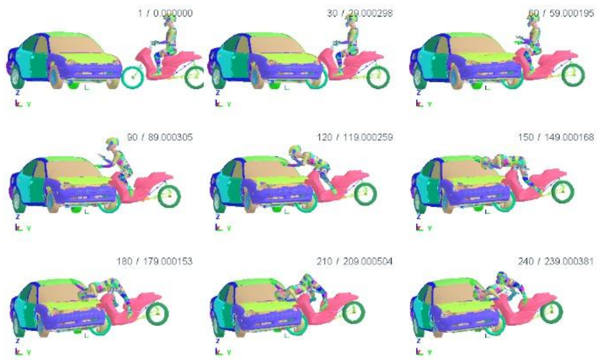

Figure 6. *Case 2 kinematics.*

The analysis of the signal from the head COG virtual accelerometer (**Грешка! Източникът на препратката не е намерен.**) shows that the biggest peak of the acceleration was around 180 ms. This data corresponds to the contour plot of the simulation (180 ms, **Грешка! Източникът на препратката не е намерен.** 6.). The calculated HIC criterion (399) is in line with the medical reports (no head injuries were reported).

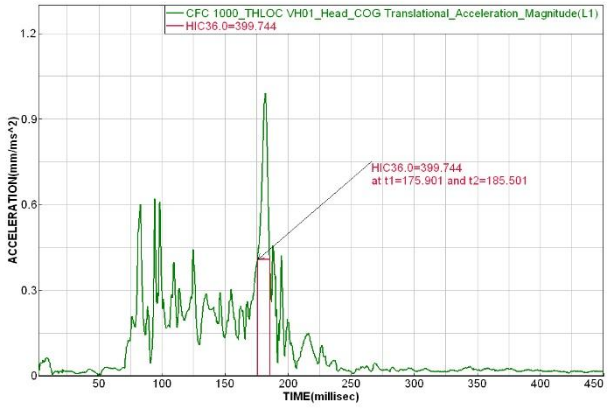

Figure 7. *Case 2 HIC assessment.*

The analysis of the Nij criterion (Figure 8.) shows that during the accident the PTW occupant was constantly inside the safe corridor for the neck. This is in line with the medical examination – neck injury was not reported.

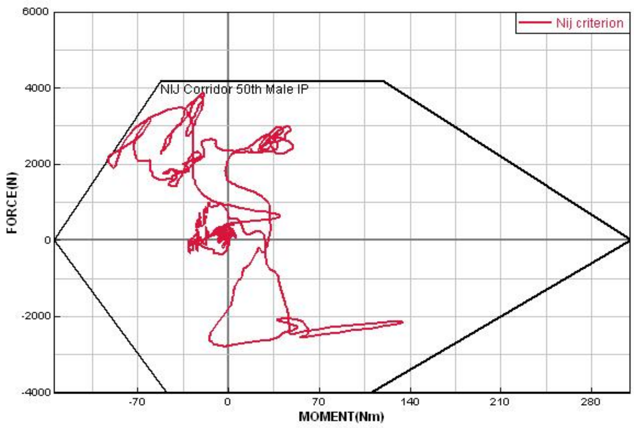

Figure 8. *Case 2 Nij corridor.*

3. Conclusions

The VPS Virthuman shows in simulated cases a good recreation of the PTW occupant kinematics. Its main advantage is the scaling possibility and acceptable calculation time. In comparison with more complicated FEM human body models (THUMS, GHBMC), the Virthuman is easier to position. However, it should be mentioned that even improved MBS models of the human body can only be used to evaluate predefined and existing injury criteria. They do not have any built-in mechanisms for real injury simulation (e.g. lung puncture). From the engineering point of view, numerical accident simulation can be a booster for PPE development teams, but, as with every tool, they are only as good as the people who use them.

4. Acknowledge

The work has been supported by the research project CZ.02.1.01/0.0/0.0/17_048/0007280 Application of Modern Technologies in Medicine and Industry and the internal grant project SGS-2019-002 Biomechanical models of human body, biological tissues and biomechanical processes with application in industry and medicine

4. References

[1] R. Noon, Introduction to forensic engineering, Boca Raton: CRC Press, 1992.

[2] R. Noon, Forensic engineering investigation, Boca Raton: CRC Press, 2001.

[3] J. Vychytil, J. Manas, H. Cechova, S. Spirk, L. Hyncik and L. Kovar, "Scalable Multi-Purpose Virtual Human Model for Future Safety Assessment," *SAE Technical Paper,* Vols. 2014-01-0534, 2014.

[4] G. Kasanický and P. Kohút, Analýza nehôd jednostopových vozidiel, Žilina: Žilinská univerzita v Žiline, 2000.

[5] D. Kirk, Vehicular accident investigation and reconstruction, Boca Raton: CRC Press, 2000.

[6] A. Chwla and S. Mukherjee, "A Road Crash Reconstruction Technique," *Institute of Engineers Journal,* vol. 91, pp. 3-8, 2010.

[7] R. Eppinger, E. Sun, F. Bandak, M. Haffner, N. Khaewpong, M. Maltese, S. Kuppa, T. Nguyen, E. Takhounts, R. Tannous, A. Zhang, and R. Saul, "Development of Improved Injury Criteria for the Assessment of Advanced Automotive Restraint Systems - II," NHTSA, 1999.